NTNU

Norwegian University of
Science and Technology

Finite Element Approach to Estimating Shell Properties of Nanoparticle-stabilized Microbubbles

Daniel Thor Morton

Mechanical Engineering
Submission date: June 2016
Supervisor: Bjørn Helge Skallerud, KT

Norwegian University of Science and Technology
Department of Structural Engineering

Preface

This thesis was supervised by Professor Bjørn Helge Skallerud of the Biomechanics group at the Department of Structural Engineering at the Norwegian University of Science and Technology (NTNU). This project was conducted throughout a 20 week period during the spring of 2016 and is a requirement for the degree of Master of Science at NTNU.

Acknowledgements

I would like to thank my supervisor Professor Bjørn Helge Skallerud for making this thesis possible and for providing good guidance, advice and insights throughout the project. He has been a great help while interpreting results, suggesting the direction of progression and facilitating meetings and resources.

I would also like to thank Senior Engineer Astrid Bjørkøy at the Department of Physics for providing the experiment data available, valuable discussions and insight regarding the experimental data and setup. Professor Catharina Davies and the rest of the Department of Physics were all helpful in evaluating the progress and provided much sought after information about nanoparticle and microbubble properties. Research scientist Dr. Torodd Berstad and the Structural Impact Laboratory (SIMLab) were very helpful in facilitating and allowing me to run simulations on their cluster.

Last but no least, many thanks to my friends and family who have supported me along the way.

Trondheim, 2016-06-10

Daniel Thor Morton

Abstract

The application of nanoparticle-stabilized microbubbles(NP-MB) for localized drug delivery is a new and promising method for enhancing the effectiveness of administered drugs. The NP-MBs move through the vascular system before being destroyed by a targeted acoustic pressure field. The NP-MBs shell properties determine the in-vivo response. Accurately determining the shell properties will allow us to better understand the complex phenomenons which make this method an valuable medical tool. This thesis aims to utilize finite element modeling in order to better estimate the NP-MBs shell properties.

Previous thesis work at the Department of Physics has conducted a series of experiments where individual NP-MBs were compressed by an atomic force microscope. The bubbles force-displacement curve is the basis for estimating the shell properties. This system is considered equivalent to a parallel plate compression of a hollow sphere. A finite element model representing a NP-MB model was simulated in Abaqus. Running different parameters and material models the, Yeoh material model was identified as a better alternative to the traditional linear elastic material. The linear elastic model resulted in a poor fit to the experimental data, with the bubbles different Young's modulus ranging from $25MPa$ to $112.5MPa$. By using Yeoh form the non-linear response of the NP-MBs were better replicated. The Yeoh form, typically used for rubber materials, allow a non-linear stress-strain relation. The different bubbles were simulated with the Yeoh material and the estimates for the most relevant coefficient, C_{20}, ranges between $0.96e6$ and $112.5e6$

An alternative method for estimating the shell thickness is suggested. The simulations buckling point is dependent on the dimensions and parameters of the input. By matching the buckling point of the experiments force-displacement with to the buckling point of a simulated model we are able to suggest and estimate for the shell thickness. The method indicates a negative relation between the shell thickness MB diameter. The shell thickness of the different BSA microbubbles was between 0.05 and $0.065\mu m$ The different casein bubbles have an even thinner shell with estimated thicknesses ranging from $0.05\mu m$ to beyond the lower limit ($0.25\mu m$) of the suggested method.

Sammendrag

Mikrobobler stabilisert med nanopartikler (NP-MB) er en ny og lovende metode for effektiv lokal avlevering av medisin. Bobler med medisin bundet i nanopartiklene fraktes rundt i det vaskulære systemet før de destrueres ved hjelp av målrettet ultralyd. Boblens in-vivo respons i et akustisk trykk felt er avhengig av skallets egenskaper. Etablering av disse egenskapene vil hjelpe oss åbedre forståde komplekse effektene som gjør mikrobobler til et interessant medisinsk verktøy. Denne masteroppgaven undersøker om bruken av element metoden kan bedre estimeringen av skallets egenskaper.

Tidligere masteroppgaver ved Institutt for Fysikk har utført en rekke relevante eksperimenter. Individuelle mikrobobler har blitt trykt sammen ved hjelp av et atomic force microscope. Den resulterende kraft-forskyvningskurven beskriver boblens stivhet. Denne stivheten har opphav i skallets egenskaper, for eksempel tykkelse og elastitetsmodul. Det eksperimentet anses som ekvivalent til komprimering av en hul sfære mellom to flate plater. Numeriske modeller tilsvarende dette systemet ble modellert i Abaqus. Ved åkjøre et utvalg parametere og materialmodeller finner vi at en Yeoh materialmodell beskriver den eksperimentelle kraft-forskyvningskurven bedre enn det lineærelastiske alternativet. Boblenes estimerte elastitetsmodul for the lineærelastiske materialet ligger mellom 25 og 112.5 MPa. Den lineærelastiske modellen predikerer dårlig responsen til de eksperimentelle dataene. Ved bruk av Yeoh materialmodell kunne vi tilpasse dens koeffisienter slik at simuleringsresultatene stemte bedre overens med de eksperimentelle dataene. Yeoh, typisk anvendt pågummi, tillater en ikke-lineær spennings-tøynings kurve. Yeoh materialets koeffisienter ble funnet for de forskjellige boblene. Den mest relevante parameteren, C_{20}, ligger mellom $0.96e6$ og $120e6$

Det blir foreslått en alternativ metode for etablering av skalltykkelse. Ved åsammenligne buklingspunktet i et eksperiment med et simulert buklingspunkt kan vi estimere skalltykkelsen. Ved åtilpasse simuleringens forskjellige parameter vil vi kunne si noe om for eksempel skalltykkelsen. Denne metoden indikerer en negativ avhengighet mellom skalltykkelse og boblediameter. Skalltykkelsen for de forskjellige BSA boblene ligger mellom 0.05 og $0.065\mu m$. Casein boblene har et enda tynnere skal med estimerte tykkelser mellom $0.05\mu m$ og metodens nedre grense ($0.25\mu m$) for estimering.

Contents

Chapter 1

Introduction

Coated microbubbles comprising of drug loaded nanoparticles(NPs) have successfully been used to deliver drugs to a targeted area in vivo. The material properties of the microbubble(MB) shell play an important role in predicting the response of a MB. Accurately describing the response will help tune the MB to ensure that they are able to circulate to the targeted area. After reaching the target area they must exhibit the desired response at the application of an ultrasound field. Considering NP-MBs the predictable destruction is also required in order to successfully deliver the targeted drugs. One significant parameter is the material stiffness of the MB shell. Assuming a linear elastic material Moe[1] estimated the Young's modulus (stiffness) for several NP-MB batches produced by SINTEF. By pressing on individual bubbles with a flat surface he obtained a force-displacement ($F-\Delta$) curve for each bubble. Using various established theoretical models for compression of spheres, an estimate for the stiffness was determined. This thesis aims to better estimate the parameters of the NPMB as the $F-\Delta$ curves exhibits behaviour which is not explained in the analytical theories. Based on available information about the MBs we constructed and simulated an approximate representation. This model seems to exhibit some elements of the experiment behavior, for instance buckling which is the reduction in force required to continue compression. We were able to suggest a method for inferring shell thickness and we fitted the simulation parameters to the experimental data thus obtaining a new estimate for the shell stiffness. The initial non-linear effects seen in the experiment data can not be described with a linear elastic material model. The the non-linear Yeoh material model provides a better fit.

1.1 Background

An ultrasound contrast agent(UCA), also referred to as coated microbubbles, improves the contrast between the agent and surrounding medium in an ultrasound image. The primary purpose in a clinical setting has been to distinguish circulating liquid from the stationary tissue and hence better show the flow of blood. Combining the concept of UCAs with drug loaded NPs and creating NP-MBs we are able to locally deliver medicine by destroying the bubbles in a targeted area. Increasing the concentration of drugs in a specific area enables a greater uptake and utilization of the administered drugs.

By better understanding the shell properties we can further develop simulation accuracy. This will allow us to move towards using numerical tools in explaining the complex interactions which govern efficient drug delivery. An example would be drug delivery through the blood-brain barrier(BBB) in which ultrasound (US) medicated delivery have shown increased uptake. By being able to accurately represent the response of both bubble and barrier, more efficient bubbles can be developed. By estimating the shell properties we are one step closer to modeling the dynamic response of a microbubble.

Today there are two primary methods employed to estimate MB shell parameters. Atomic force microscope (AFM) compression of a bubble and acoustic characterization. The AFM experiment gives a direct measurement of an individual bubble's stiffness. The acoustic characterization is an indirect way of estimating the properties. It is based on measuring the energy attenuation in a bubble solution and fitting theoretical model parameter from which it is possible to derive shell parameters. AFM studies previously conducted in other masters theses are the background for this master thesis. We try to better describe the material properties with additional insight gained from numerically simulating the problem. There are numerous similar studies idealizing the geometry of MBs and employing analytical expressions to estimate the shell properties. None have so far tried to describe the response of a NP-stabilized MB exposed to parallel plate compression.

1.1.1 Drug Loaded Nanoparticles

Nanoparticles containing drugs intended for cancer therapy have shown promise as a more effective way to deliver drug to a cancerous tissue [2]. Two primary modes of targeting cancerous tissue are currently being researched, namely passive and active. Passive targeting

utilizes the enhanced permeability and retention (EPR) effect and allows the NPs to congregate in the cancerous tissue [3, 4]. Active targeting employs specifically engineered ligands which bind to molecules present in the targeted tissue [5, 6]. The use of loaded NPs is not limited to cancer therapy and may be used with a variety of drugs, for example antiviral agents [7].

1.1.2 Ultrasound Contrast Agent

Ultrasound contrast agents have been available since 1991 (Echovist, Bayer Schering Pharma AG) but the first widely used UCA was Albunex which was introduced in 1994. As an UCA is subjected to an acoustic US pressure, their compressibility due to the gas core will scatter the US waves [8]. The boundary of two different materials will also cause US reflection, but to a lesser extent than the UCAs, hence the improved contrast. The UCAs scattered waves are then received by a transducer and an image of the tissue and UCAs can be created[9]. Typical UCAs are gas bubbles with a diameter of $1-10\mu m$ [10]. With UCAs being similar to the size of a red blood cell they can pass through most microvessels and capillaries throughout the body. [11]. A pure gas bubble on the micron size would quickly dissolve due to the surface tension of water forcing the internal gas to diffuse quickly. UCAs are therefore coated microbubbles (MBs) where a protein, lipid or polymer acts as a surfactants in order to reduce the shell tension causing pure gas bubble to diffuse and disperse. This enables them to persist long enough to circulate and reach the desired area and be imaged.

1.1.3 SINTEF NP-MB

SINTEF is investigating the use of drug loaded NPs in an attempt to deliver drugs across the blood-brain barrier (BBB). Successful transport of NPs across the BBB was demonstrated by Andreas Aaslund of NTNU[12]. The NPs here were attached to a MB which transported the NPs to the desired area. Mechanical effects induced by ultrasound exitation of the MBs disrupted the BBB and allowed the NPs to pass. Ultrasound enhanced drug delivery of NPMBs have been investigated by Eggen et Al. [13] and it appears that US exposure of tumors has a positive effect on NP uptake.

1.2 Objectives

The overall objective of this thesis is to use finite element modeling as an alternative way of estimating the shell parameters of nanoparticle-stabilized microbubbles (NP-MBs). Previous estimates of shell parameters are based on theoretical models derived for a linear and small deformation regime. These fail to capture non-linear behaviour seen in experimental data. NP-MBs are a relatively new field of science which means many highly relevant parameters are unknown. By simulating the compression of a NP-MB model we aim to determine shell parameters by fitting the simulations variables to match the experimental data. Using Abaqus as the finite element (FE) software we aim to gradually improve a simulation model until a representative behaviour is seen.

1.3 Limitations

The history of NP stabilized MBs is short. The number and magnitude of unknown factors present a big challenge in trying to conclude and estimate any one phenomenon or parameter. As the size of the components is on the nanometer scale it is hard to generalize any observed phenomenon. There are uncertainties in the accuracy of measurement or imaging and there is a distribution pertaining to any physical quality of the NP-MB. For the available data we only have limited knowledge about the parameters of each component. Currently the assembly process, geometry and local properties of a NP-MB have not been established. One of the most significant unknown properties is the shell thickness. This is a crucial aspect of determining the shell stiffness and ultimately the bubble response both in vitro and in vivo.

1.4 Approach

Due to the difficulty of acquiring accurate knowledge of NP-MB structure and geometry the Abaqus model evolved in relation to the available information. Initial models were based on a homogeneous, constant thickness spherical shell where as later and final models incorporates protruding NPs. The primary results of interest is the $F-\Delta$ curve of a parallel plate compression scenario, representing the experiment. Python scripting in Abaqus was utilized as it allowed for automation of simple repetitive tasks as the models were iterated.

The scripting allowed the modeling of numerous NPs distributed across the MB without the tedious practice of placing each one by use of the Abaqus CAE GUI. The material properties of the models were then adjusted so the simulations results would behave like the MBs in the experiment.

1.5 Theories for Estimating the Young's Modulus

Moe [1] covered four different models for determining the Young's modulus of spheres and shells. These are briefly discussed below and their individual assumptions are presented. Figure 1.1 illustrates the various theories given equivalent boundary conditions for the applicable variables.

1.5.1 deJong Theory

N. de Jong and L.Hoff [14] presents a model for determining the shell elasticity of a coated gas bubble. The model is based on the relation between the change in bubble radius u and the pressure difference inside and outside the shell derived by Reismann [15]. The model assumes a homogeneous, constant thickness shell which is perfectly elastic. Further assuming $t << R$ the Reismanns relation can be simplified to (1.1).

$$u = (p_a - p_b) r^2 \frac{1-\nu}{2Et} \tag{1.1}$$

Moe, Chen et al.[16] and Morris [17] have employed this relation to estimate the Young's modulus from AFM data. Their method of application defines the force needed to compress the bubble as the product of the bubble stiffness and the displacement (1.2). The force exerted on the shell is defined as the pressure integrated over the shell (1.3). The pressure force is proportional with the shell stiffness and the radial change (1.4). . By solving this for K_{shell}, inserting (1.1) for the displacement u and using (1.3) in place of F_{deJong} we get (1.5). Using $K_{shell} = K_{bubble}$ they obtain an equation for the Young's modulus (1.6) as a function of the bubble stiffness.

$$F_{AFM} = K_{bubble} u \tag{1.2}$$

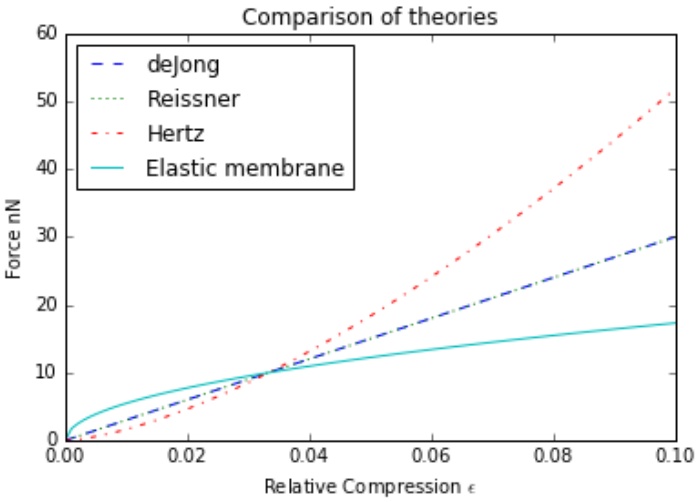

Figure 1.1: The four different theories covered by Moe are fitted to a compressive force of 10nN at a relative compression ϵ_{Def}1/30.

$$F_{deJong} = (p_a - p_b) A_{sphere} \tag{1.3}$$

$$F_{deJong} = K_{shell} u \tag{1.4}$$

$$K_{shell} = \frac{8\pi E t}{1-\nu} \tag{1.5}$$

$$E = (1-\nu)\frac{K_{bubble}}{8\pi t} \tag{1.6}$$

This way of employing the model does not describe any elements found in parallel plate compression of a MB. There is no driving hydrostatic pressure in the AFM experiment and the compression of the bubble is not equivalent to a uniform reduction in radius, which the de Jong theory is based on. The loading is illustrated in Figure 1.2. This theory is not applicable for estimating the Young's modulus from the AFM experiment.

1.5.2 Reissner Theory

The Reissner theory[18, 19] also featured by Moe has been used to estimate the Young's modulus in previous AFM studies of MBs [20, 21, 22, 17, 23]. The Reissner theory assumes a homogeneous, constant thickness, thin $t/R < 1/10$ and perfectly elastic shell. It theory is based

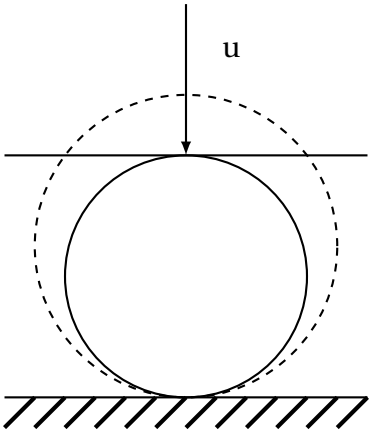

Figure 1.2

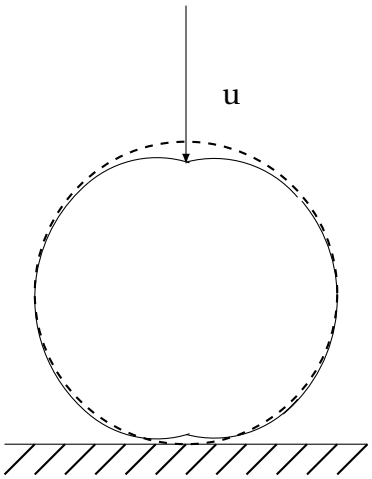

Figure 1.3

on a spherical cap with a point load acting along the axis of symmetry. The point load must be sufficently far from edge of the cap, $\phi = \sin^{-1}(1.65\sqrt{t/R})$, as the effect of edge boundary conditions can influence the stiffness. The loading condition is illustrated in figure1.3. The relation between deformation d and force F is given by (1.7). This model includes the bending stiffness of the shell which is assumed to be a driving factor in the AFM experiment. The model differs in the loading boundary condition and only for very small deformation will the loading area be comparable to a point load. Elsner et al.[21] employed a FEM analysis and showed that the Reissner theory remains a good approximation even for large contact compression, up to a few shell thicknesses.

$$d = \frac{\sqrt{3(1-\nu^2)}}{4}\frac{R}{t^2}\frac{F}{E} \tag{1.7}$$

K_{bubble} is defined by (1.8). Note that $u = 2d$. Substituting this into ther Reissner equation we can isolate the Young's Modulus as a function of bubble stiffness (1.9). As mentioned,

this equation looks at spherical cap. Relating this to the symmetrical compression of a full bubble is not explicitly stated in Moe, Morris or Buchner Santos and all three appear to only consider deformation at the one loading pole. This is despite citing Elsner et al. who suggests that a distributed load found at both the loading pole and the immobilization pole would contribute to the deformation.

$$K_{shell} = \frac{F}{u} \tag{1.8}$$

$$E = \frac{\sqrt{3(1-\nu^2)}}{4}\frac{D_0}{t^2}K_{shell} \tag{1.9}$$

1.5.3 Hertz Theory

The Hertz theory[24] is a general solution to the contact problem of two solid, homogeneous elastic spheres. This model does not yield the Young's modulus of a spherical shell but a spherical solid. Figure 1.4 illustrates the system which the Hertz theory is based on. This model will thus only be applicable for very thick shelled MBs with small deformations. By letting one sphere have an infinite radius and infinite stiffness we obtain the case of a sphere pressed onto a rigid plate (1.10).

$$d = \sqrt[3]{\frac{9F^2(1-\nu^2)}{16RE^2}} \tag{1.10}$$

By defining the relative deformation $\epsilon_{Def} = u/D_0$, using K_{bubble} as in (1.11) and modifying the original equation to consider the symmetric compression we can isolate the Young's modulus (1.12).

$$K_{bubble} = \frac{F}{\epsilon_{Def}^{3/2}} \tag{1.11}$$

$$E = \frac{12(1-\nu^2)}{\sqrt{2}D_0^2}K_{bubble} \tag{1.12}$$

The Hertz theory has been used in several studies to determine elastic properties of biological material where Buchner Santos et al. [22] looks at a MB shell and Lulevich et al. (2006) [25] looks at a cell with an internal medium. For the purpose of gaining knowledge about MBs in-vitro behaviour this model will not accurately predict the behaviour of a shell bubble.

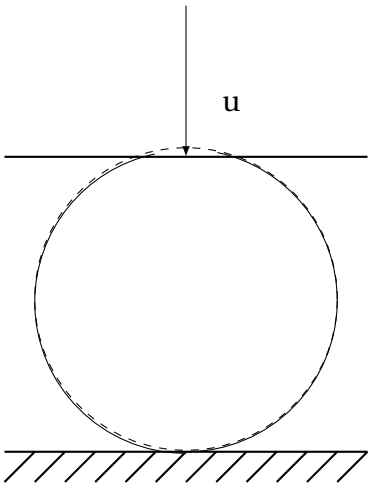

Figure 1.4: Hertz theory for compression of a solid sphere

1.5.4 Elastic Membrane Theory

The elastic membrane theory was developed by Lulevich et al. (2004)[26]. This theory also assumes a homogeneous, constant thickness and perfectly elastic shell. The system from which the theory is derived from consists of a shell filled with an incompressible liquid. When the sphere is compressed volume conservation will induce a membrane stress creating internal pressure and a reaction force opposing the compression. Lulevich also incorporates a simple consideration of the reaction force arising from the membrane bending at the separation point from the substrate/ compressing plate. This region is illustrated in Figure 1.5 and it is assumed that all bending occurs over a length comparable to the thickness

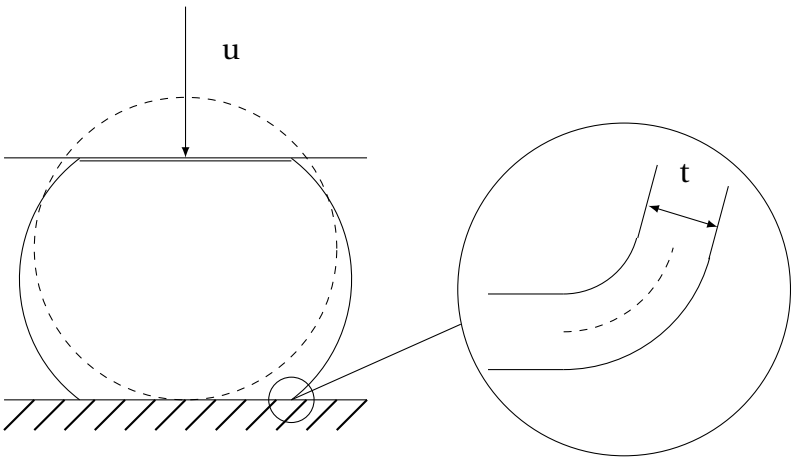

Figure 1.5

The total reaction force from both membrane bending the volume conservation membrane stretching is given in (1.13) where $\epsilon_{Def} = u/D_o$. Since the MBs investigated have a

gas core the contribution from the volume conservation will be smaller and is neglected (see Section 3.2.1). By defining K_{shell} in (1.14) the resulting expression relating bubble stiffness to the Young's modulus is given in (1.15)

$$F = \frac{\pi}{2\sqrt{2}} E t^2 \epsilon_{Def}^{1/2} + 4\pi E t R_0 \epsilon_{Def}^3 \tag{1.13}$$

$$K_{shell} = \frac{F}{\epsilon_{Def}^{1/2}} \tag{1.14}$$

$$E = \frac{2\sqrt{2}}{\pi t^2} K_{shell} \tag{1.15}$$

Chapter 2

Experiment Details

2.1 Background

The AFM-data available is from NP-MBs produced by SINTEF and is denoted GB-161 and GB-167. In order to simulate the NP-MBs it is important to describe the boundary conditions(BCs) as accurately as possible, allowing us to make reasonable simplifications. This chapter covers the fabrication processes of a general NP-MB and we briefly discuss how various properties impact the modeling of the MBs. The information gathered about fabrication process and component properties is an aggregate from different batches including batches produced after the batches we have data for. Is has be difficult do gather accurate information about the GB-161 and 167 batches specifically. Different aspects are covered by information gathered from equivalent or similar processes. The details of the experimental setup are also covered, again aiming to accurately describe the conditions in which the bubbles are tested. These BCs are equally important to the MBs own BCs when we try to analyse the data provided by the AFM.

2.1.1 Nanoparticle

The data presented by Moe[1] utilizes MBs with Targ 121 NPs. Two phases of respectively fat-soluble and water soluble components are mixed. The fat-soluble mixture comprises PACA (poly(alkyl cyanoacrylate)) monomers and dyes(Nile Red®) while the water soluble mixture consists of PEG(Polyethylene glycol) and surfactants. An ultrasound field is applied and a miniemulsion is obtained. The microspheres polymerizes and creates solid particles. The size of the NPs is dependent on the intensity of the energy field. The PEG aggregates in the

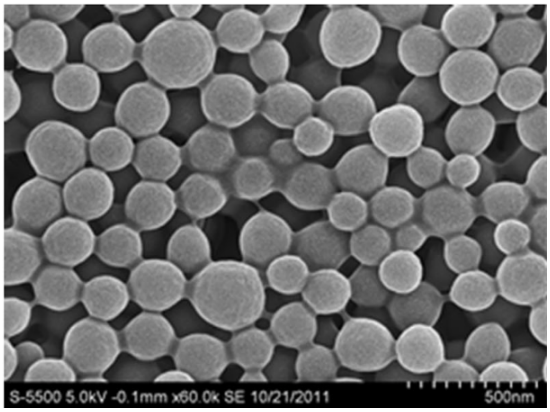

(a)

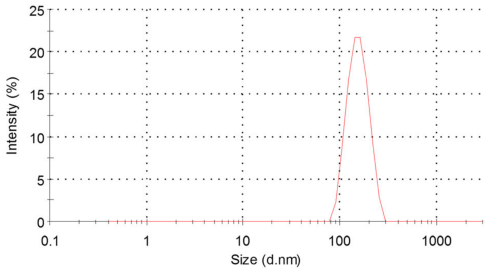

(b)

Figure 2.1: (a) STEM image of PEGylated PBCA NPs. (b) Hydrodynamic diameter of PEGylated PBCA NPs. Both images gathered from Mørch et al.[27]

interface of the emulsion particles giving rise to a surface which SINTEF assumes to consist of 50:50 hydrophobic/ hydrophilic polymer ends. The average size of these SINTEF NPs is typically 200nm. This information is gathered from Astrid Bjørkøy (Department of Physics). The specific size distribution of the Targ 121 NPs is not know, but it is expected to be similar to later NP batches. Figure 2.1b shows a size distribution of NPs with the majority of NPs being in the 100-200nm range.

Studies done after Moe's experiment cover NPs in greater detail and provide valuable insight into later generation NP and MB properties. Figure 2.1a shows poly(butyl cyanoacrylate) based NPs imaged by scanning transmission electron microscopy (STEM). Mørch et al. [27] characterizes the ζ-potential of the NPs which dictates the degree of repulsion. The ζ-potential is found to be between -15 and -35mV depending on PEGylation. This suggest that the NPs will not rapidly aggregate and hence some degree of separation between the NPs is assumed.

2.1.2 Formation of MBs

To make NP-MBs a solution of NP(1%) and protein (Casein or BSA, 0.1-1.0wt%) is mixed and any air is displaced by the desired gas. The sealed container is then stirred with an ultraturax. The stirring speed determines the average size of the formed MBs. A representative distribution for GB batch NP-MBs is shown in Figure 2.2. We do not have the distribution of the GB batches we have data from. The GB161 and GB167 MBs are all made with casein.

The gasses employed by SINTEF vary by batch and include carbon dioxide (CO_2), air and

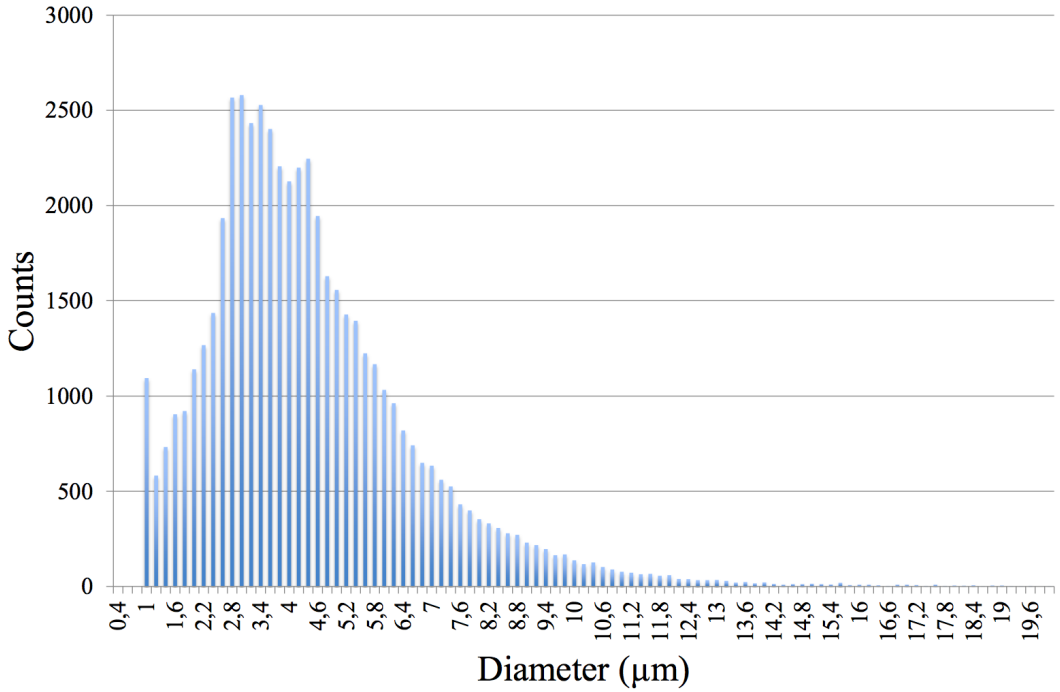

Figure 2.2: Distribution of GB169 NP-MBs having a mean size of 3.92μm. Graph gathered from G. Moe[1].

perfluorpropane (C_3F_8). Due to the NP-MB having a stable size over time the internal pressure is assumed to be at equilibrium with the surrounding medium. A heavier gas like the perfluorpropane with a higher molecular mass reduces dissipation rate out of the MB. This prolongs the relaxation time when the MB is produced. It is assumed that the rate of loading is too fast for any significant amount of gas to diffuse out due to an increased internal pressure. Borden & Lango [28] suggested a dissolution relation for MBs based on diffusivity of the gas. The Epstein and Plesset equation [29] couples the change in radius to the diffusion of gas out from a bubble. By adding a term for the diffusivity through the shell, Borden & Lango were able to describe the time dependent dissolution of a coated MB. Since diffusion through the shell is dependent on the shell thickness it is assumed that the relatively large expected thickness of a protein MB causes very little gas to dissipate throughout the experiment and can hence be neglected. For the purpose of the AFM experiment the type of gas is irrelevant since any internal pressure effect is only dependent on the relative change in volume, not the molecular weight of the gas.

Azmin et al[30] investigated the stabilizing effect of gold NP coated MBs. Two primary dissolution limiting effects were suggested; NPs limit the effective surfactant area where the gas can diffuse through and the tension between NPs being reduced as the packing density

increases. The NPs reduce the speed of bubble dissolution until a critical particle concentration is reached and a stable MB diameter is maintained. The MBs in this study were produced with only a surfactant(PEG-40-stearate) as opposed to the SINTEF MBs which uses protein as the surfactant. The stabilizing effect of protein might be different than that of only surfactant and the stable radius of the SINTEF MBs might have a substantially different critical particle concentration. The primary interaction between NPs and the protein is assumed to be electrostatic and Mørch et al. [27] hypothesises that the NPs act as a hub from which a network of higher order protein multimers can extend along the gas-water interface.

2.1.3 Surface Properties

The surface geometry of a later generation MB was inspected with Scanning Electron Microscope (SEM) imaging. Figure 2.3 shows the surface of the bubble. The GB194 batch depicted below uses a BSA protein surfactant. No casein NP-MBs were imaged with SEM and we lack a detailed surface image of these. To be able to capture the images the surface had to be coated with Au. This was done with chemical vapor deposition. The thickness has not been disclosed but being similar to the imaging process of NPs in Figure 2.1a we can assume a coating thickness of around 5nm.

Other NPs produced by SINTEF, presumably with similar methods, have approximately 0.088 PEG chain pr nm^2 [27]. The PEG chains on the surface of the NPs will affect the contact region of the $F-\Delta$ curves. Pasche et al. [31] studied the compressibility of various PEG densities and found that a PEGylated sphere compressed by a flat SiO_2 surface show an exponential rise in force as the relative separation goes towards zero. Considering data with similar PEG coverage (0.1 nm^{-2}) and scaling with our NP diameter the effect of PEG compression has a range of about 5nm. No further significant compression of the PEG layer occurs after about 1.6nN (Scaled to NP D=200nm). The effect of PEG chain compression is therefore neglected. The low PEG coverage of the NPs combined with the small 200nm diameter also limits the number of PEG chains in the initial contact area, which also indicates that the effect of PEG compression should be neglected. A study done by Kowalczyk et al. [32] shows that HSA, presumably similar to BSA which is used in Finnøy's NP-MBs, is able to coat the surface of a poly(styrene/acrolein) microsphere. This could mean that any PEG originally present on the NPs are suppressed or otherwise impacted by the surfactant protein

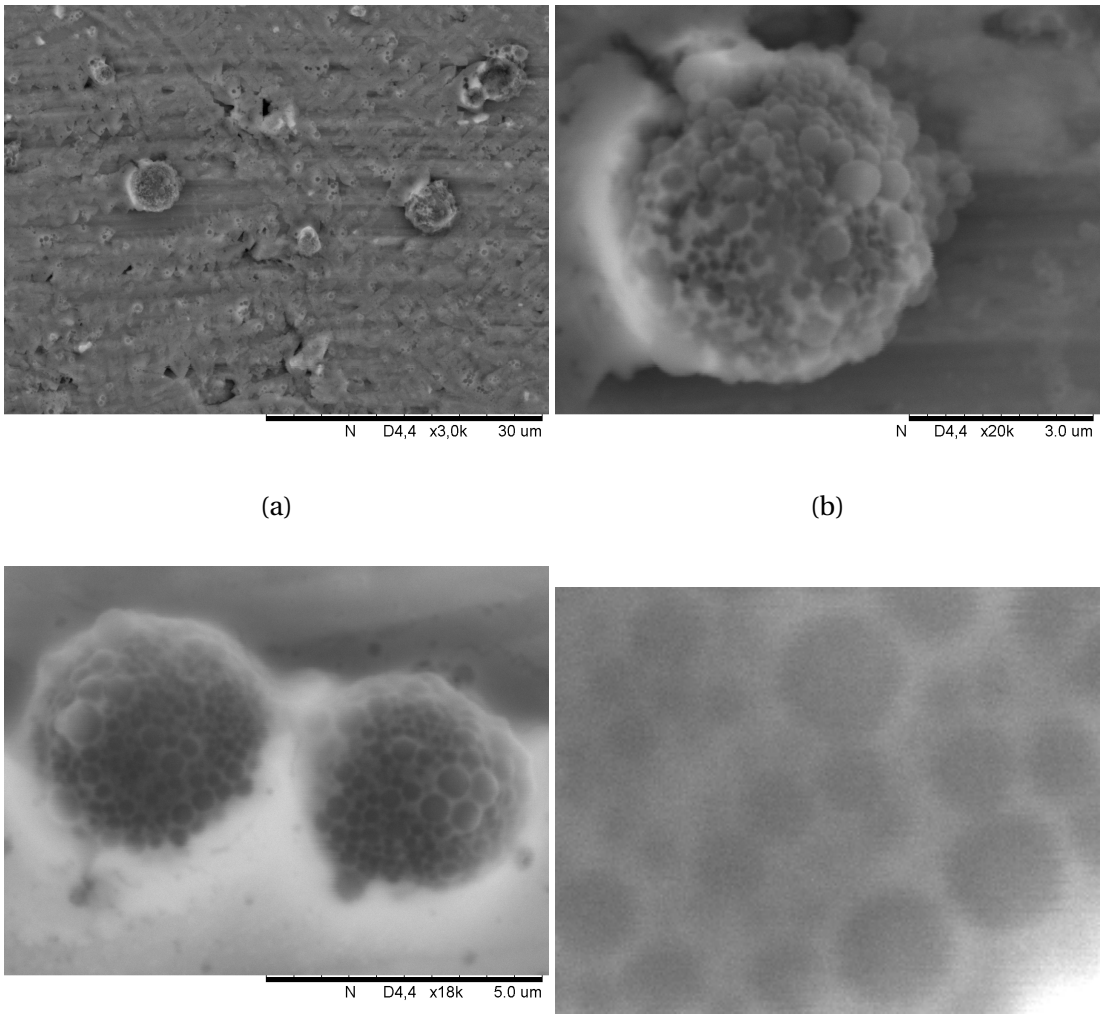

(a) (b)

(c) (d)

Figure 2.3: (a-c) Scanning electron microscopy picture of NP-MB batch GB194. (d) Detailed view of NP-MB surface in Figure 2.3c. Pictures kindly provided by A. Bjørkøy

2.1.4 Shell Thickness

The shell thickness of the GB batch MBs has not been accurately determined. Moe has employed a thickness of 300nm based on Figure 2.4. The confocal laser scanning microscope allows focusing on a cross section of the sample and illuminates the fluorescent particles in the NPs. From the image we can assume a single layer of NPs. It is not possible to say anything about the thickness of the non-fluorescent medium surrounding the NPs.

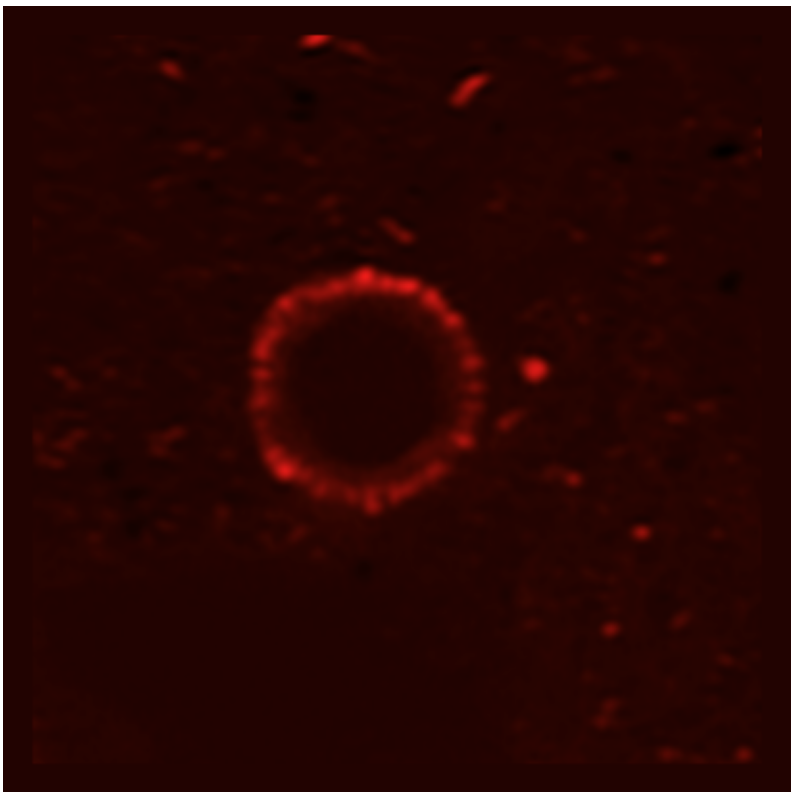

Figure 2.4: Confocal Laser Scanning Microscope image of a GB batch NP-MB [1]

Assuming one layer of NPs around the bubble and looking at Figure 2.3d, we can infer that the protein matrix thickness is significantly thinner than the NP diameter. Pure protein MBs like Albunex have been covered in a variety of literature. The molecular mass of the human serum albumin(HSA) is similar to the bovine serum albumin(BSA) and one can imagine similar size and behaviour of the protein. Albunex shell thickness has been suggested by several sources; 15 nm [33], 25nm by de Jong et Al. [14] and 30-50nm by Barnhart et al.[34]. Of the mentioned studies Barnhart et al. best covers other aspects of the bubble properties and the 30-50nm is hence assumed to be a good estimate.

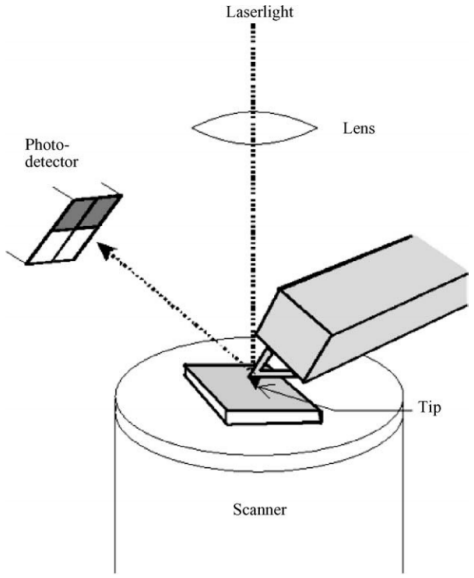

Figure 2.5: Schematic of an atomic force microscope[35]

2.2 AFM

Figure 2.5 illustrates how an AFM operates. Light is aimed at the cantilever tip and reflected up to a four node photo-detector. As the cantilever bends due to any force, direct force or otherwise, the intensity in each quadrant of the photo-detector changes. Knowing the movement of the cantilever the force is computed as the product of the cantilever displacement and the cantilever stiffness k_c. The AFM tip and MBs are submerged in about 2mm of water. The hydrostatic pressure from submergence is negligible The viscous damping of the system moving through the water is assumed negligible due to no distinguishable hysteresis being present as the AFM cantilever approaches and retracts from the MBs. The AFM base was driven at 0.5Hz which corresponds to a scan rate of $6\mu m/s$.

2.2.1 MB Immobilization

The hard base of the AFM setup is a glass dish (WillCo-dish®, WillCo Wells, BV, Amsterdam, Netherlands) coated with branched polyethylenimine(PEI). This allows the MBs to be attached and kept in place as the AFM measurement is conducted. The thickness and material properties of the PEI layer has not been studied. Deflection sensitivity tests preformed on the glass surface show deflection of the cantilever tip for separation less than 10nm. Further deformation of the base is not evident. It is not know how much of the deflection leading up to contact is due to various repulsive forces and how much is from compression of the

PEI. Chen et al. [16] studied a similar system with a PLL coating and found no significant deformation of the substrate. Van der Waals forces are typically present only closer than $0.3-0.6nm$ and is neglected. The magnitude of any potential electrostatic repulsion is not know. Figure 2.6 shows the force on the cantilever as a function of separation from the glass base. On the stiffest bubbles, 10nm this base sensitivity can reduce the effective bubble compression with as much as 10%. This effect is compensated for in all subsequent plots. This was done by defining the sensitive region of 10nm and inverting the sensitivity curve. The yielding substrate is a function of the compressive force. This will yield a stiffer MB due to the sensitivity curve being done with a rigid cantilever tip. This tip has an initial angle of 11° and the end is presumably square. This will penetrate the substrate easier than the immobilized MB, hence a siffer calibrated MB $F-\Delta$ curve is obtained. Overall the effect of the substrate deformation is small and the softer solution is assumed to be appropriate.

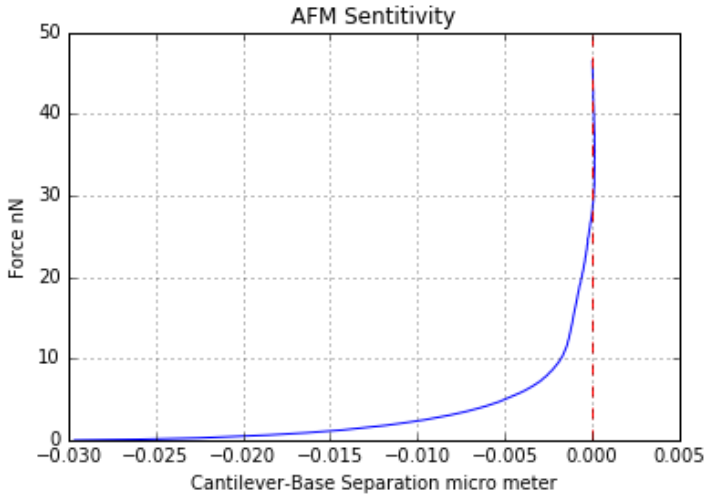

Figure 2.6: Deflection of cantilever as it approaches the glass base. Raw data provided by A. Bjørkøy

The MBs were attached to the coated glass base by overfilling a container with NP-MB solution and placing the coated glass base on top, illustrated by Figure 2.7. The NP-MBs rise upwards due to the buoyancy and adhere to the coating. Due to the small size of the MBs the buoyancy in the piconewton range meaning that the MBs see little or no deformation as they adhere to the glass base.

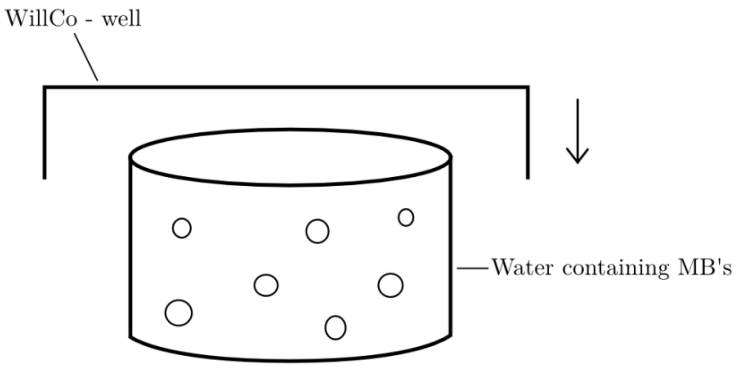

Figure 2.7: Immobilisation of NP-MBs to a coated glass base, illustration gathered from Moe

2.2.2 AFM Tip

A flat cantilever of type NSC12 (MicroMasch, Madrid, Spain) was utilized. The shape of the cantilever is shown in Figure 2.8. The coating of the AFM tip is not known.The cantilevers used had a stiffness, k_c, between 0.3-1.0 N/m. The exact stiffness of each cantilever used was determined by thermal tuning. This method looks at the cantilevers response to thermal noise, determining its resonance frequency and hence deriving its stiffness from the geometry and now known eigenvalue. [35]. The flat cantilever is oriented at an 11° angle relative to the horizontal base. The cantilever tip was placed over the selected MB as illustrated in Figure 2.9. The bubble was positioned as close to the end of the tip as possible to assure that the overhanging portion did not come in contact with the base

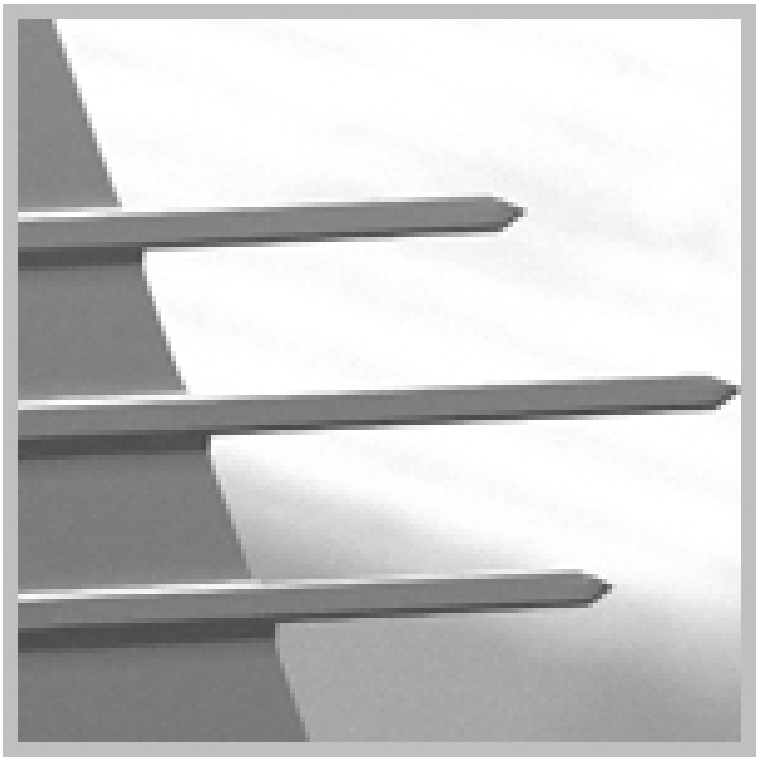

Figure 2.8: ZEM image of 37 series AFM tip (MicroMasch, Madrid, Spain) which has replaced the NSC12 tip used in Moe's experiment.

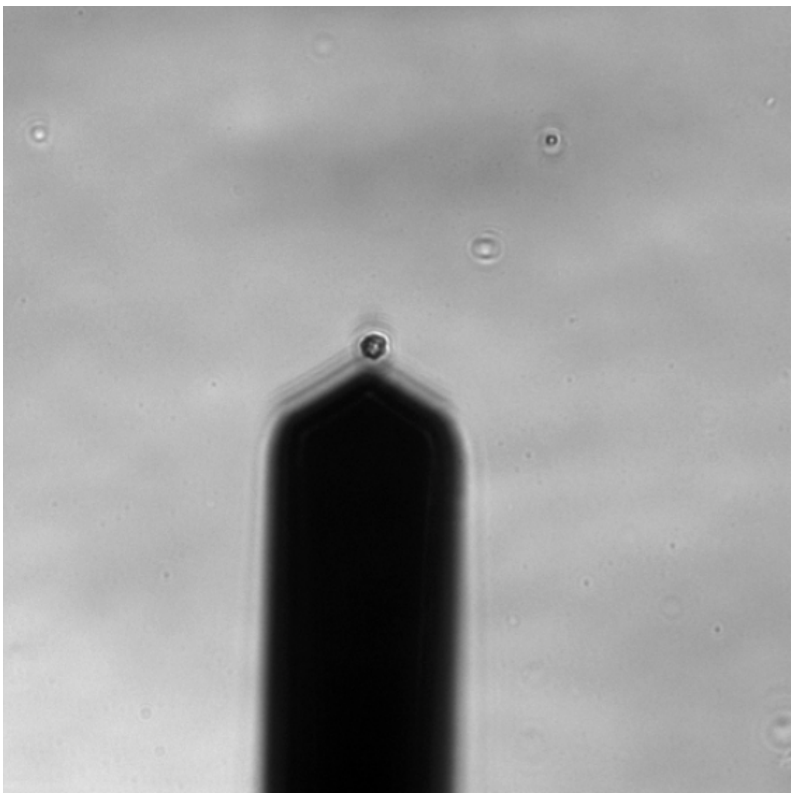

Figure 2.9: NSC12 flat AFM tip over NP-MB[1].

2.3 Experimental Data

The numerical data available is from Moe's experiments. Finnøy did a similar study in 2013 and this data is only available as $F-\Delta$ plots found in his thesis. Both data sets will be used to draw insight from the simulations and other theoretical considerations. Some bubbles exhibit a notable hysteresis in the measurement data. This effect was difficult to accurately compensate for due to instances of binding in the unloading curves. Simply taking the average would disrupt the initial true $F-\Delta$ response. As only about half of the bubbles show any significant sign of hysteresis it was decided to only analyse the $F-\Delta$ curve as the cantilever tip was approaching.

2.3.1 Determining contact point

Processing of the numerical data from Moe's experiment follows. The AFM output provided by A. Bjørkøy consists of the force on the cantilever and the location of the of the base relative to an unknown reference. To get the compression of the NP-MB we have to first subtract the cantilever deflection from the base location and then set the point of contact. The cantilever deflection is the product of the force and the inverse of the cantilever stiffness k_c. This enables us to separate the deflection of the cantilever and the compression of the MB. Moe does not indicate how he has determined the contact point but if he adopted Finnøys approach the contact point is defined as "where the force between two consecutive data points changes with more than 0.5nN". The validity of method is questionable as you might loose any non-linear effects present in the initial part of the compression. Several alternative methods have been suggested by others performing similar AFM measurements on variuos structures. Chen et al. [16] uses the same approach as McKendry et al. [36], defining the contact point as where "the measured force increased by 2% relative to the baseline value for 10 consecutive data points". Other methods include fitting to analytical solutions eg. Hertz model for a solid sphere [37], direct analysis (visual) of the changing derivative [38] and algorithm based numerical analysis of the FD-curve by Jaasma et al. [39].

As the data set presented was rather inconsistent the chosen method was a combination of direct analysis and the algorithm based numerical analysis presented by Jaasma et al. This method defines the contact point as the last point where derivative of the cantilever deflection is zero. The root of the derivative is approximated by fitting a linear function to a

predefined region and finding its root. Jaasma defines the region as 15-40% of the maximum value of the derivative. A strict region like this did not work for our available data. Direct analysis was incorporated to find an appropriate region to fit the linear function. This is exemplified in Figure 2.10b. As the data supplied was not smooth the cantilever deflection data was filtered with a Savitzky-Golay filter[40]. The filter fits a polynomial to a predefined frame of data points by the linear least squares method. The center value of the local polynomial becomes the filtered value at the coinciding midpoint of the range. The local polynomial is then recomputed after moving the frame one data point to the right. The first derivative of the cantilever deflection is computed by a second order central difference scheme. The last step was truncated as the backward difference method employed at the end caused significant discontinuities. This smoothing ended up hiding details of the cantilevers contact point. The contact point determination was done with the unfiltered cantilever derivative. This also a reasonable approach as the linear regression smooths any local noise. The smoothing was only applied to the final $F-\Delta$ curve. The last few data points of each measurement might be inconsistent due to the base switching from approaching to retracting. The FD curves of all the available numerical data are plotted in Figure 2.11. The two different $F-\Delta$ curves presented in Figure 2.12 are gatherd from Finnøy's Master Thesis [41]. All of Finnøy's MB compression plots are included in Appendix A.

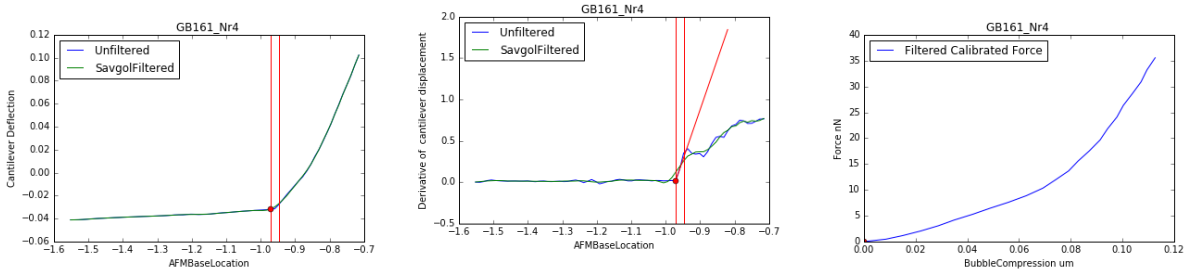

(a) Cantilever deflection.

(b) Derivative of cantilever deflection.

(c) Calibrated F-Δ curve.

Figure 2.10

The $F-\Delta$ curves from both Moe and Finnøy are from the last of 20 compressions. Finnøy determined that most of the bubbles underwent some small degree of permanent change in the first few compressions. As the number of compressions increased the response converges. From the data presented by Finnøy any permanent buckling is not evident.

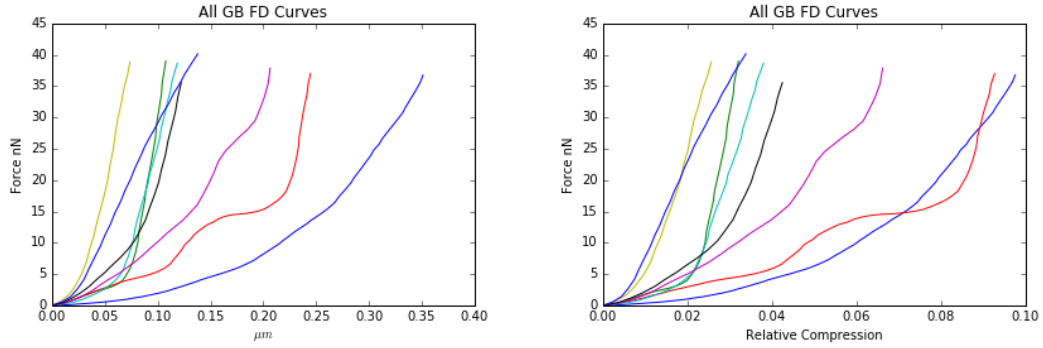

(a) (b)

Figure 2.11: (a) Absolute compression and (b) relative compression $F-\Delta$ curves from Moe's experiments, data provided by A. Bjørkøy (Department of Physics)

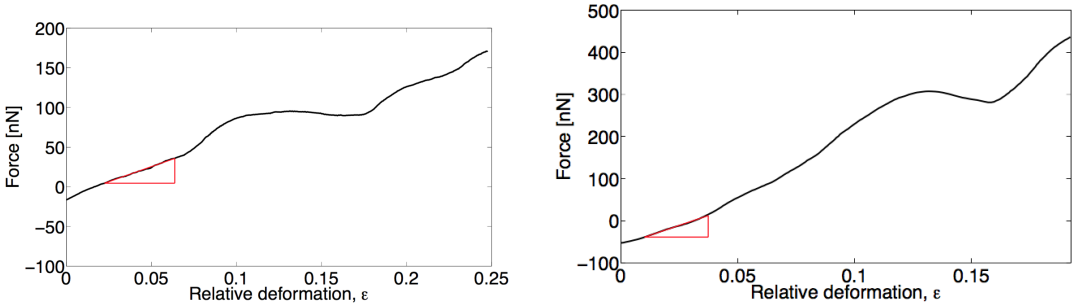

(a) (b)

Figure 2.12: (a) YM-73 BSA abd (b) YM-73 Casein $F-\Delta$ curves gathered from Finnøy's Master Thesis [41].

2.3.2 Determining Bubble Diameter

The diameter of Moe's NP-MBs is determined by counting the number of pixels the bubble spans as viewed through a microscope. The pixel width is $0.24\mu m$. This causes significant problems with regards to the accuracy as the indicated diameter has an error of +- $0.24\mu m$. This translates to 6% of the GB169 mean diameter and a 17% error over the data sets span $(4.08 - 2.64/mum)$. This is quite a significant error and it could have an influence on the accuracy of the results.

Chapter 3

Simulation

In this chapter we cover the model used to obtain simulation results. Two different shell geometries are presented. The smooth MB geometry employs a constant shell thickness where as the nubbed shell is based on spherical caps protruding from the MB surface. The constant thickness shell did not work well. It did not seem to describe the alternating second derivative found in some of the F-Δ curves. SEM images of later generation NPs indicate a non-smooth surface.

3.1 Abaqus

To numerically model the NP-MBs the finite element program Abaqus (Dassault Systèmes Simulia, Waltham, MA) was used. This program allows solving non-linear systems with both implicit and explicit solvers. All presented simulations were considered quasi static and run in Abaqus/Standard utilizing the implicit solver.

3.1.1 Input dimensions

Abaqus does not employ any specific dimensions but requires consistency across input units. Any length dimension is denoted in μm, any pressure is denoted kPa, thus any force is denoted in nN.

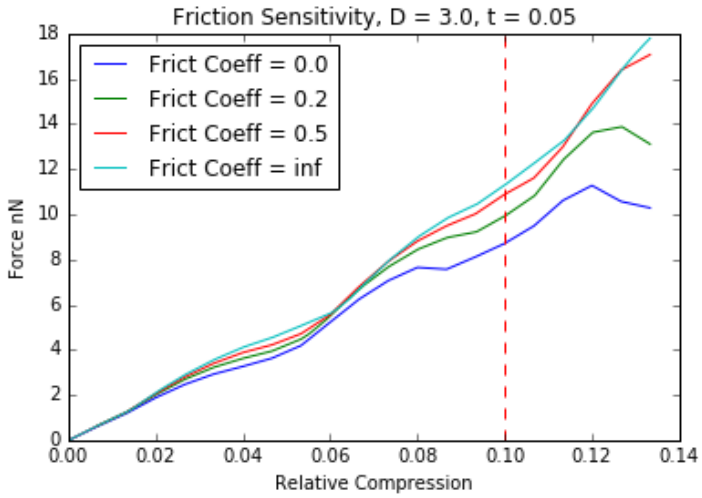

Figure 3.1: The influence of plate-bubble friction.

3.2 Boundary conditions

MB compression between the AFM cantilever and the glass base are simplified to compression between two analytically rigid surfaces, as the PEI glass coating already has been compensated for. The angle between the AFM tip and the base described in Section 2.2.2 was also neglected as preliminary simulations showed only a small difference between angled surfaces and parallel surfaces, seen in Figure 3.2. Note that this comparison uses a rough friction formulation in order to keep the bubble from squeezing out between the symmetric, angled plates. The magnitude of the force is similar and the phase shift is attributed to the plate contacting the NP as at slightly different angle. To restrain the model with the angled plate without imposing unreasonable boundary conditions on the base of the MB, a rough friction formulation was used. The subsequent simulations are all parallel plate compression. The influence of friction between the MB and plates is relevant for the final stiffness. Due to lack of information about the interaction properties of the NP-MBs and the surface of the cantilever tip, a frictionless interaction was used all subsequent simulations. From Figure 3.1 we can see that in increase in friction causes a stiffer response.

3.2.1 Effect of Internal Pressure

Compression on a closed volume like the MB will increase the internal pressure and induce a strain the shell. An increase in internal pressure will oppose the compressing force. The influence of the internal gas being compressed can first be evaluated as a simple system,

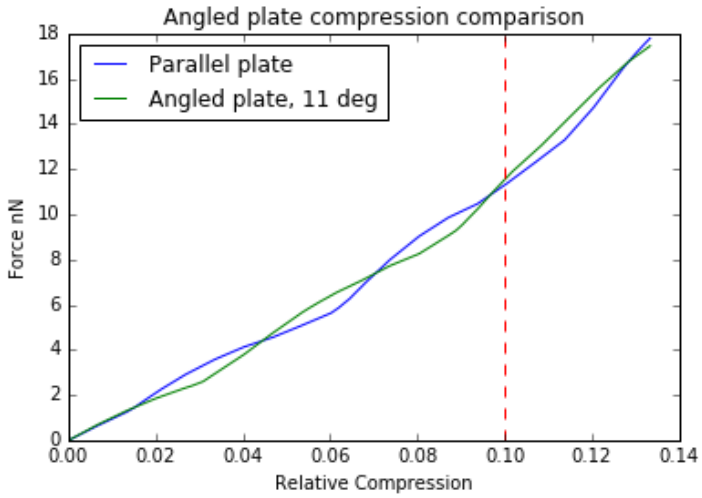

Figure 3.2: Angled compression of a sphere compared to parallel plate compression.

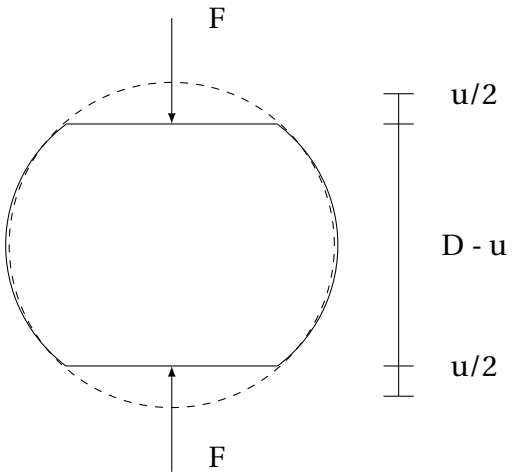

Figure 3.3

illustrated in Figure 3.3. The two spherical caps are subtracted from the initial volume while maintaining a constant amount of gas.

If we assume a rigid shell with no bending stiffness, then the internal overpressure is a function of the volume reduction (3.1). The normalized force resulting from the overpressure applied to a circular cross section corresponding to the spherical cap size is given by equation (3.2) where $\epsilon_{Def} = u/D$ is the relative compression. Figure 3.4 plots the normalized force function and shows the exponential increase as the volume is compressed. Note that this is a worst case estimate. In reality the increase in pressure will also cause the membrane to stretch and the resulting force will be less.

$$\frac{p_{overpressure}}{p_1} = \left(\frac{2}{2-\epsilon_{Def}^3(3\epsilon_{Def}^{-1}-1)} - 1\right) \tag{3.1}$$

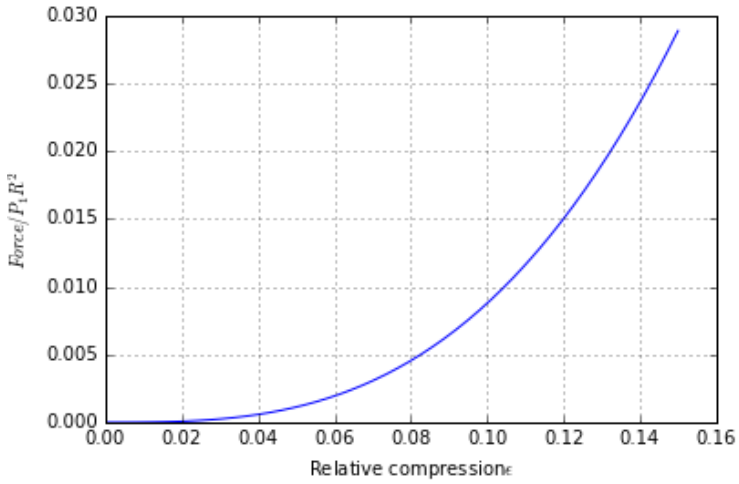

Figure 3.4: Normalized force resisting compression as a function of relative deformation ϵ_{Def} YLABEL

$$\frac{F}{p_1 R^2} = \frac{-\epsilon_{Def}^6 + 5\epsilon_{Def}^5 - 6\epsilon_{Def}^3}{2 - \epsilon_{Def}^2(3 - \epsilon_{Def})} \tag{3.2}$$

These plots and functions enable us to estimate a critical compression after which the internal pressure becomes significant. Most of Moe's simulation data are in the sub $40nN$ range. Assuming an equilibrium pressure of $101kPa$ and a MB diameter of $3\mu m$ and that we want a worst case pressure influence of less than 5%. The relative compression must then be less than approximately 0.061. Simulation data shows that the effect on the MBs is small for a relative compression $\epsilon_{Def} < 0.1$.

The effect of the internal pressure was simulated for a generic nubbed sphere. The fluid cavity interaction in Abaqus creates a volume element from a surface element on the part and a reference node, in this case the center of the sphere. As the geometry changes the volume of the surface-node element will change accordingly and impose a pressure according to ideal gas law under isothermal conditions. The ambient pressure was set to 101kPa and the temperature was set to $20°C$.

Figure 3.5 illustrates the difference between one simulations with internal pressure and one without. The diameter of the bubble is $3\mu m$, thickness of $50nm$ and a Young's modulus of 24 MPa. This Young's modulus corresponds to the estimated stiffness of a GB bubble, not including the effect of internal gas. Internal pressure is not included in subsequent simulation as it drastically increases computational cost and the effect is negligible for the relative deformations seen in Moe's experiment.

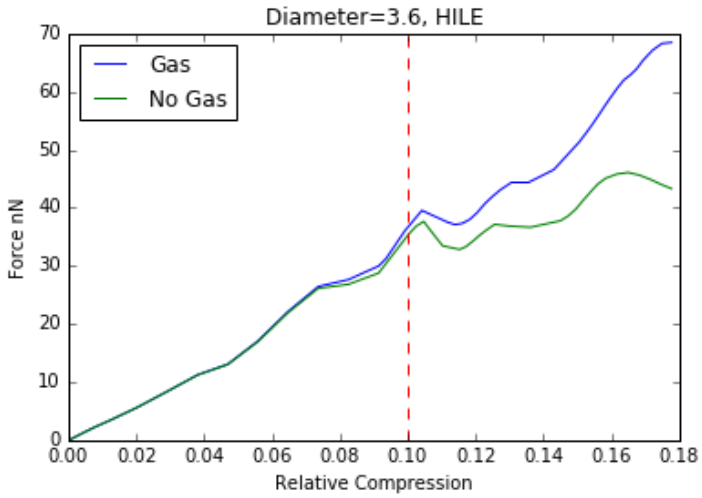

Figure 3.5: Simulation with and without the effect of internal compressible gas.

3.3 Material models

The two material model used in the simulations was the linear elastic, homogeneous and isotropic material (HILE) and the Yeoh form. A typical example for the HILE materia's application would be small deformations of steel or other metals. The Yeoh material model is a hyperelastic material. Hyperelastic materials are often used to describe the stiffness of rubbers and polymers and has the ability to alter the shape of a non-linear stress-strain relation. Conceptually this might be a better fit to our problem of modeling proteins which exhibit an exponential stress-strain response. The two models are covered in further details below.

3.3.1 Compressibility

The Poisson ration, ν, is the degree of compressibility and an incompressible material has $\nu = 0.5$. The compressibility of biological material is typically assumed to be nearly incompressible [42, 43] with a Poisson ratio ν of $0.45 - 0.49$. We opt to use $\nu = 0.45$ as BSA and casein are biological material and no specific compressibility was found for either protein. By choosing $\nu < 0.49$ we also avoid the need to employ hybrid elements. It is uncertain what Poisson ration was employed by Moe. Finnøy used $\nu = 0.4$ based on another study employing PCBA NPs but using an organic surfactant(Triton X-100, Merch, Germany)[44] instead of protein based.

3.3.2 Linear Elastic

The linear elastic property means that the material exhibits a linear relation, the stiffness matrix $\boldsymbol{E}$, between the strain vector $\boldsymbol{\epsilon}$ and the stress vector $\boldsymbol{\sigma}$ seen in equation (3.3). The tensile modulus, the linear coefficient relating stress and strain is called the Young's modulus and is denoted E. A linear elastic simulation is compared to a non-linear tensile modulus in Figure 3.6.

$$\boldsymbol{\sigma} = \boldsymbol{E}\boldsymbol{\epsilon} \tag{3.3}$$

3.3.3 Yeoh

When using Yeoh form for the material model we have a greater ability to alter the stress strain curve. The investigation into the Yeoh material is motivated by the $F-\Delta$ curve of proteins[45, 46, 47, 48] which exhibits an exponential stress strain relation. Kawakami et al.[49] show the successive unbinding of a protein as intermolecular bonds are broken. These unbinding steps are neglected as the MBs in this thesis are composed of denatured protein (direct communication with Andres Åslund, Department of Physics, NTNU). The degree of denaturation is not known.

The Yeoh form is an energy function for a hyperelastic material. The incompressible material version is presented in equation (3.4) where I_1 is the first strain invariant of the right green strain (3.5).

$$W = C_{10}(I_1-3) + C_{20}(I_1-3)^2 + C_{30}(I_1-3)^3 \tag{3.4}$$

$$I_1 = tr(\boldsymbol{C}) = \lambda_1^2 + \lambda_2^2 + \lambda_3^2 \tag{3.5}$$

The right Cauchy-Green deformation tensor is given by (3.6) where **F** is the deformation gradient given in (3.7). Incompressible behaviour is defined by $J = det(\boldsymbol{F}) = 1$

$$\boldsymbol{C} = \boldsymbol{F}^T\boldsymbol{F} \tag{3.6}$$

$$\boldsymbol{F} = \frac{\partial \boldsymbol{x}}{\boldsymbol{X}} \tag{3.7}$$

The 2. Piola Kirchoff stress is found by differentiating the energy function with respect

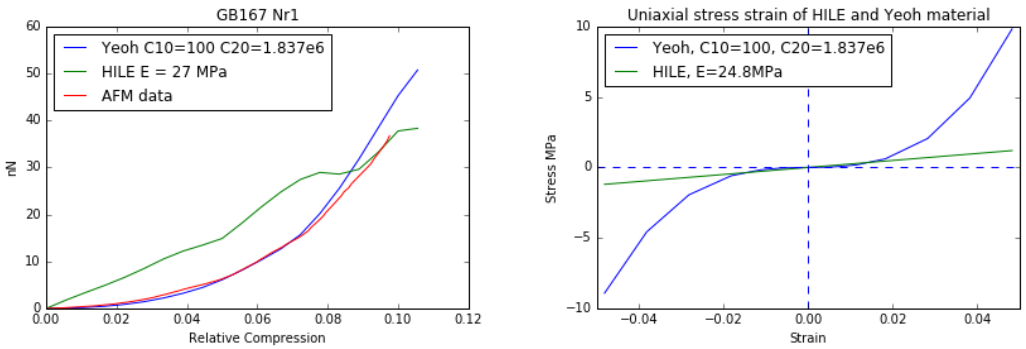

(a) $F-\Delta$ curve for the two material properties.

(b) $\sigma-\epsilon$ curve for uniaxial strain.

Figure 3.6: Stress-strain plot for the two material models. These have the same parameters as the $F-\Delta$ plot.

to the Green strain (3.8). The 2. Piola Kirchhoff expresses the current deformed force on the undeformed unit area and is energy conjugate to the Green strain.

$$\boldsymbol{S} = \frac{\partial W}{\partial \boldsymbol{E}} \tag{3.8}$$

The coefficients of the Yeoh form allow us to tune the initial slope as well as the coefficients for the second and third order relation. In order to replicate the exponential effect of the It was not possible to successfully alter the Poisson ratio of this material to anything other than $\nu = 0.5$. The incompressible material was used in combination with an incompressible element formulation. The initial stiffness is chosen very low in order to represent the small slope of the initial regions of the experimental data.

The large deformation of a nubbed shell, $D_{MB} = 3.0, t_{Shell} = 0.05$, with Yeoh material is shown in Figure 3.7.

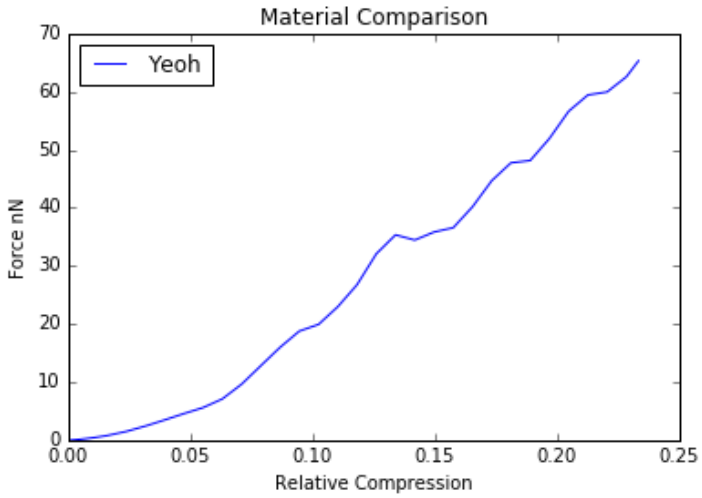

Figure 3.7: $F-\Delta$ curve of a nubbed shell with Yeoh material. Model geometry: $D_{NP} = 0.2\mu m$, $D_{MB} = 3.0\mu m$, $t_{Shell} = 0.05\mu m$, packing density = $\frac{15}{\pi}\mu m^{-2}$. Material properties: $C10 = 100, C20 = 800e3, C30 = 0, D1, D2, D3 = 0$

3.4 Smooth MB Shell

Plate compression of a spherical shell is an extensions of the sphere-sphere contact problem covered by Elsner et al.[21]. Initial simulations were run on half the sphere with an axis-symmetric model using solid elements. The pre- and post-deformation geometry is shown in Figure 3.8 As compression continues the plate will stabilize the shell until a critical point is reached. This point is not possible estimate with the simulations as it is strongly dependent on the magnitude of imperfections introduced. Imperfections were found by a linear perturbation buckling analysis with a unit overpressure on the entire outer surface of the sphere. The first two buckling modes were then introduced as imperfections with a magnitude 10^-3 of the buckling modes. If the imperfections were too small then the simulation would crash due to time step length limits. The effect of internal pressure was not included here. This would drive an exponential increase in compressive resistance for $\epsilon_{Def} > 0.1$.

Typical $F-\Delta$ curves are presented in Figure 3.9. The simulations were run with a constant Young's modulus $E = 30MPa$, a fixed diamter $D = 3.0\mu m$ and a equal maximum relative deformation $\epsilon_{Def} = 0.2$

This simulation model was not pursued to great extent due to the missing initial non-linear region and input dependence on the buckling point

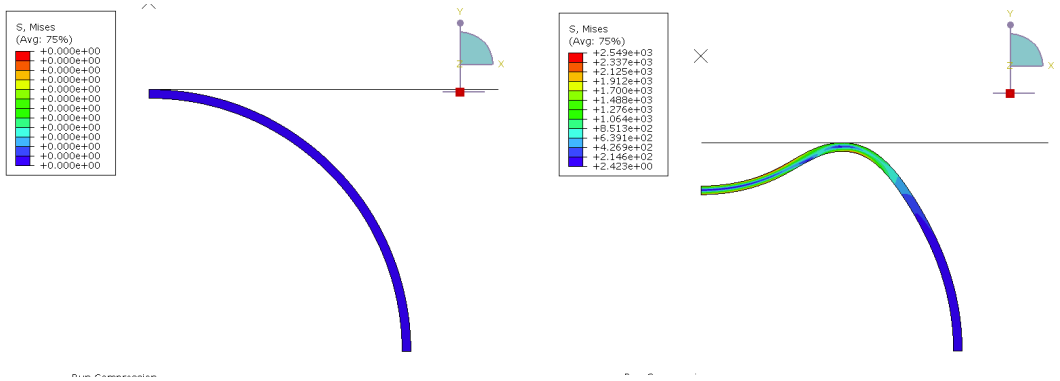

(a) (b)

Figure 3.8: (a) Geometry of the undeformed axis-symmetric smooth sphere and (b) the deformed geometry.

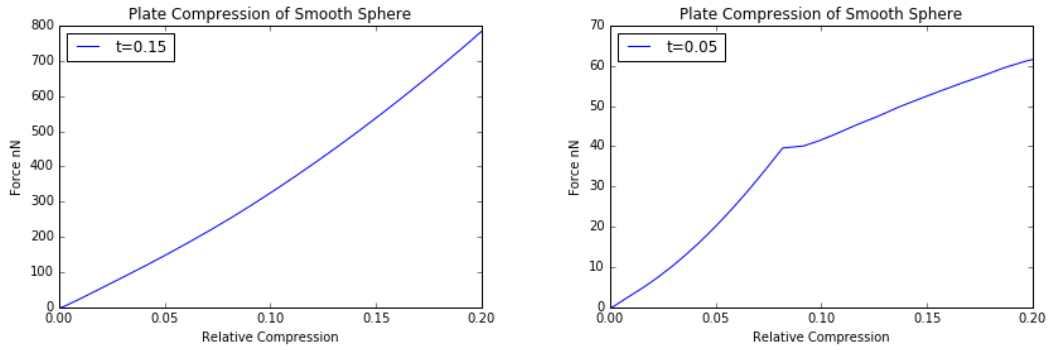

(a) (b)

Figure 3.9: Typical $F - \Delta$ curves with two different thicknesses.

3.4.1 Mesh and Element Properties

For simplicity the models are run with rectangular elements, 10 elements across the thickness. Maintaining a longer than taller aspect ratio is important in order to avoid integration errors of the shear force. 10 elements across the thickness also helps alleviate this issue. A quadratic axis-symmetric element, CAX8, was used. Reducing computational time was not a priority due to the small number of elements. The contact method used was a master surface to slave nodes. The slave nodes are not allowed to penetrate the master surface. This does cause some inaccuracy with the courser mesh as the elements edges are still allowed to penetrate. To alleviate this one could have employed a surface to surface formulation which forces the average of the full elements penetration to zero. The surface to surface formulation was not used as an accurate initial contact description was desired and a surface approach would have allowed penetration of the topmost node.

3.5 Nubbed MB Shell

3.5.1 Geometry

The geometry of the NPMB is based on a hollow sphere where its thickness represent the surfactant found in the gas-liquid interface. A number of smaller solid spheres are distributed on this interface. Based on the the SEM images in Figure 2.3 and the assumption that the NPs assemble in the interface with approximately equal parts on either side of the gas-liquid interface the locations of the NPs can be determined. The largest cross section of the NPs are placed on to the middle surface of the shell as illustrated in Figure 3.10. A general NP diameter was chosen to be 200nm and they are modeled approximately equidistant from each other. The distribution of NPs and hence equidistant points on a sphere has no analytical solution except for the few platonic solids (polyhedras with flat, equal faces) with 4, 6, 8, 12 or 20 vertices.

There are a variety of methods for approximating equidistant points on a spherical surface. The Thompson problem[50], minimizing the potential of electrostatic energy in a system of electrons, can be solved numerically and will yield an optimal distribution. Rakhmanov et at. [51] fits N equal area parts onto the spherical surface where the area corresponds to a diameter which does not interfere with neighboring areas. A computationally less expensive

approach and the approached used in the NP-MB Abaqus models employ a Fibonacci lattice [52]. The sphere is divided into N-2 equally spaced circles and points are assigned consecutively on the circles with an angular increment equal to the golden angle ≈ 137° [53]. The golden ratio, on which the golden angle is derived from prohibits periodicity in the angular assignment due to its irrationality and thus clustering of points are avoided. The lattice poles were chosen 90° from the loading point as the NP distribution at the lattice poles was not at uniform as the remaining distribution. Figure 3.11 illustrates how the points are placed along a spiral. The Fibonacci lattice is used to assign NP location on the NP-MB shell and was chosen due to its implementation simplicity and available documentation. The NP packing density on the MB shell was sett to $\frac{Q}{4\pi}\mu m^{-2}$ where the the area of the MB shell is $A = 4\pi r^2 \mu m^2$ and Q ranged from the lesser packed (55) to the very tightly packed (75). A general packing $Q = 60$ was utilized on all simulations except the sensitivity study of NP packing. This was motivated by the SEM images in chapter 2 and the magnitude of the zeta-potential which indicates some degree of repulsion between the NPs.

The construction of the geometry was done with Abaqus' python interface which allowed automation over the variables like MB diameter, shell thickness, NP diameter, NP location, material properties, mesh resolution, element properties and the loading boundary condition. This enables efficient iteration over the parameters, allowing us to quickly evaluate each variables significance.

Only one quarter of the sphere is run in Abaqus. Assuming a symmetric compression on both the top and bottom we can cut the sphere in half. This is still a large model which would take a long time to run. Assuming an approximately symmetric compression around plane parallel to the loading axis further reduces the solver matrix. This assumption is an approximation as the NPs are not symmetrically distributed. A further halving would enhance any errors relating to the NPs being split by the symmetry plane. This would be especially relevant during the initial deformation as a errors pertaining to local lack of symmetry would be multiplied four times as opposed to two. Ideally, the NPs would be a separate entity from the MB shell. The polymer NPs are presumably stiffer than the protein shell they are embedded in. During the time of modeling, no efficient way of separating the NPs from the shell was achieved. The NPs were therefore assigned the same material properties as the shell. This was assumed reasonable due to the NPs being solid, such that there would be little local deformation. As the force increases more NPs will come in contact with the compressing plate

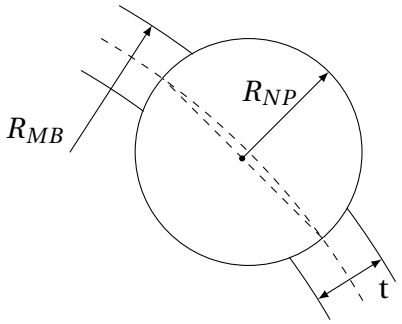

Figure 3.10: Location of NP centroid in relation to the shell cross section

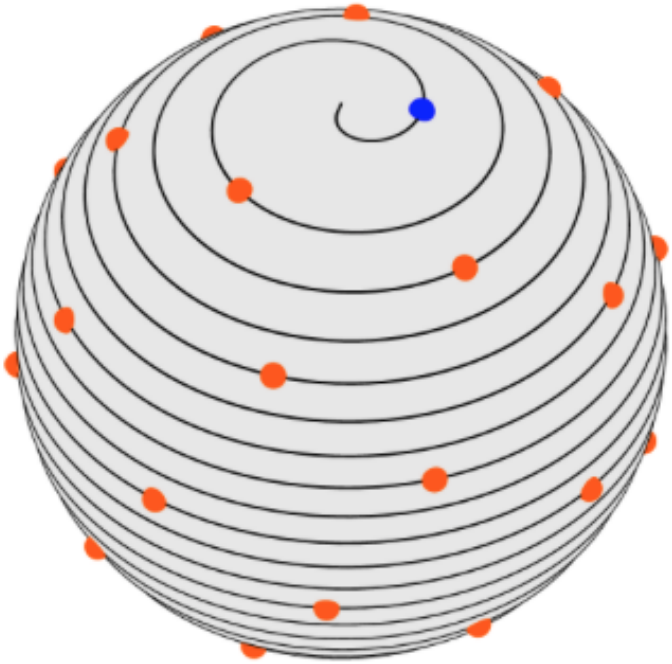

Figure 3.11: The points are placed along a spiral pattern. Figure taken from Keinert et al. [54]

and the compressive force will be distributed. The deformation of a single NP is negligible compared to their respective rigid body motion.

3.5.2 Mesh and Element Properties

The complex geometry and number of smaller solid spheres on the surface warranted the use of Abaqus' automatic mesh tool. To accommodate the solid spheres a tetrahedral element illustrated in Figure 3.13 was chosen. Of the available elements the C3D10I element has superior performance on contact problems [55] but will not work with incompressible material. The C3D10I element is called the "improved surface stress visualization tetrahedral". This is due to the 11 point integration scheme with integration points being located

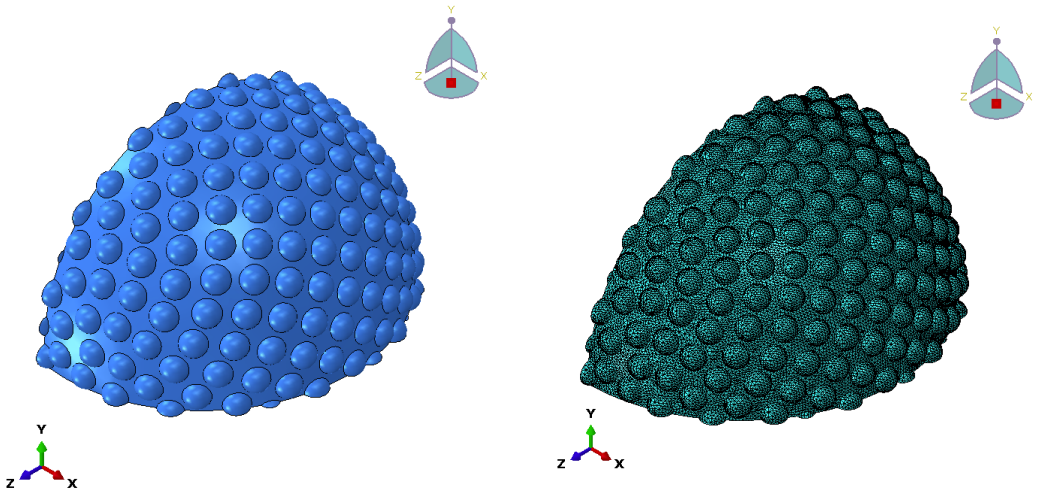

(a) (b)

Figure 3.12: (a) Complete quarter model with a diameter of 3.0μm and (b) complete quarter model mesh.

at the edges of the elements with one point in the middle. Since we are not interested in the stress distribution at the contact points, but rather the total transferred force, a C3D10 element was chosen for the HILE material model and C3D10H was used with the Yeoh material model. The hybrid element formulation alleviates both volumetric locking problems and oversensitive pressure response to small deformations which arise with incompressible materials [56]. This was required for the use of the incompressible Yeoh material model. The second order shape functions also improve the representation of surface stresses and the curved geometry found at the contact points between the NPs and the rigid plate. A detailed view of the NP-MB mesh is shown in Figure 3.14b. Figure 3.16 illustrates the change in response as a function of different mesh sizes. This plot illustrates that the larger elements produce a reasonable estimate. The mesh sensitivity was not run for a finer mesh due to the rapidly increasing size of the solver matrix. As the NP-MB model is cut along the symmetry plane, smaller geometries might have to be described. Many of the GB bubbles required a mesh size of maximum 0.02 in order for the automatic meshing tool to function. This approximate mesh size was used for all the final simulations.

Deformation Geometry

The deformation geometry of the nubbed shell is shown in Figure 3.15.

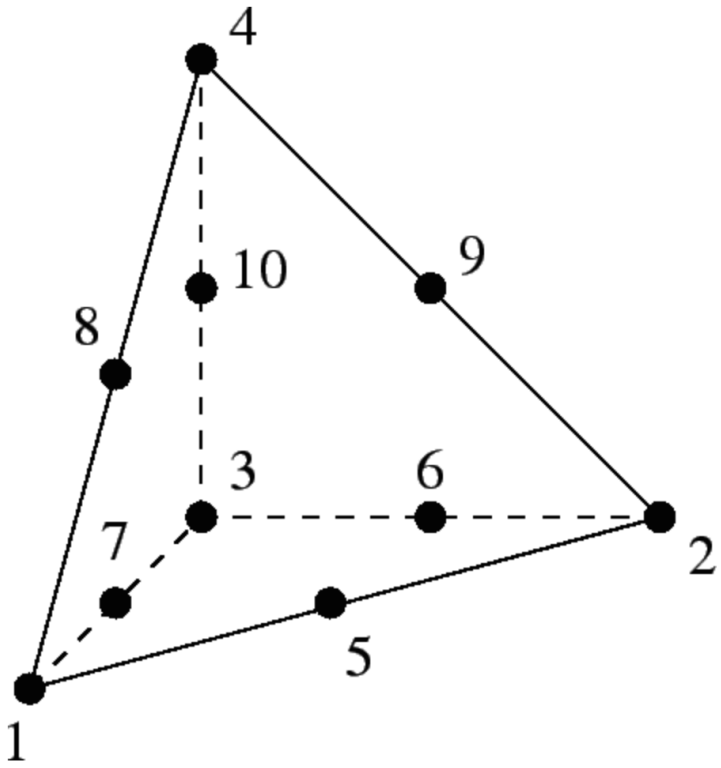

Figure 3.13: C3D10 element

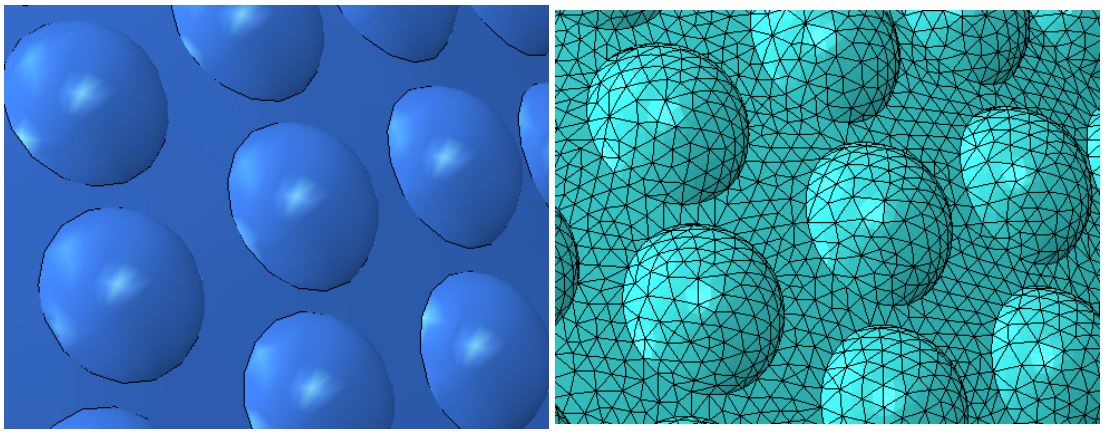

(a) (b)

Figure 3.14: Detailed view of the embedded NP geometry, unmeshed (3.14a) and meshed with therahedra elements (3.14b). $D_{NP} = 0.2\mu m$, $D_{MB} = 3.0\mu m$, $t_{Shell} = 0.05\mu m$ and packing density = $\frac{15}{\pi}\mu m^{-2}$.

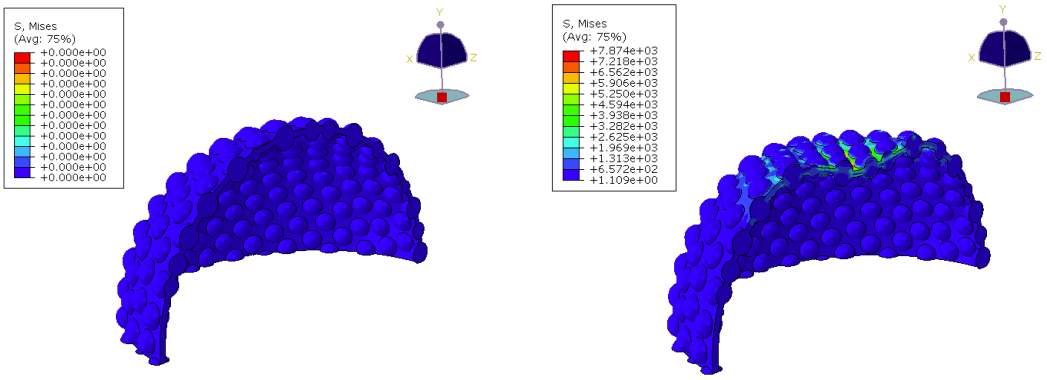

(a) (b)

Figure 3.15: (a) Undeformed geometry of a nubbed shell and (b) the resulting deformed geometry

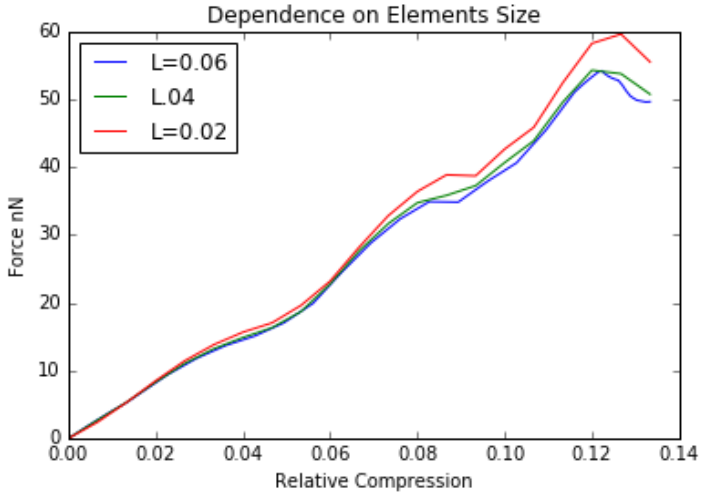

Figure 3.16: The simulated response is dependent on the mesh size. The two coarser meshes behave similarly due to both having only one tetrahedra element a cross the shell thickness.

3.5.3 Simplified MB Shell

As the diameter of the MB increased the number of elements required to accurately model the shell across its constant thickness grows to the second power. This created issues with the practical completion of the simulation. It not only took a very long time but the solver files quickly increased past 30GB and consumed all available disk space on the lab computers. A simplified geometry was therefore created. Only a spherical cap of 1/4th of the radius was given NPs. This allowed for hexahedral elements on the major portion of the model, drastically improving computational cost. The Poisson ratio was set to 0.4 during initial studies. The sensitivity study indicates that this has little impact on the stiffness of the material and the results are assumed equivalent for $\mu = 0.45$ The simplified model is illustrated in Figure

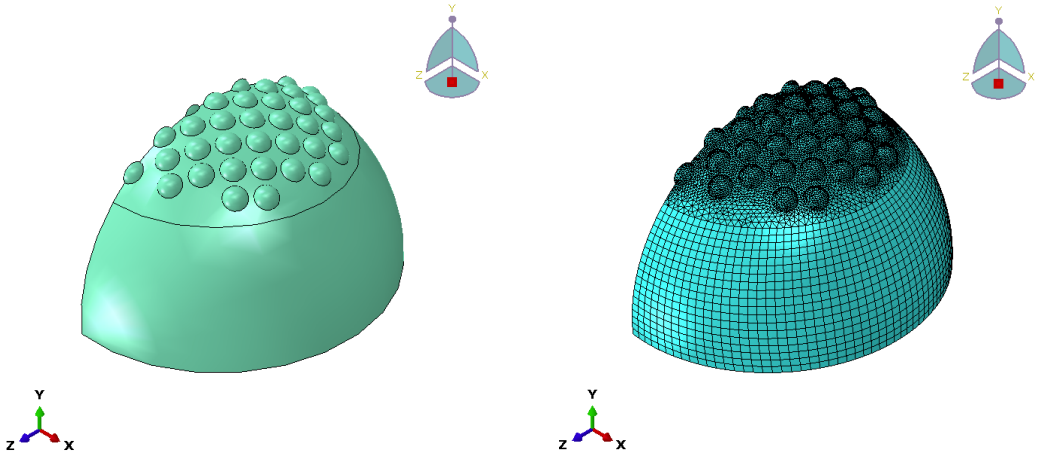

(a) (b)

Figure 3.17: Simplified model with a diameter of 3.0μm (a) and the simplified model mesh (b)

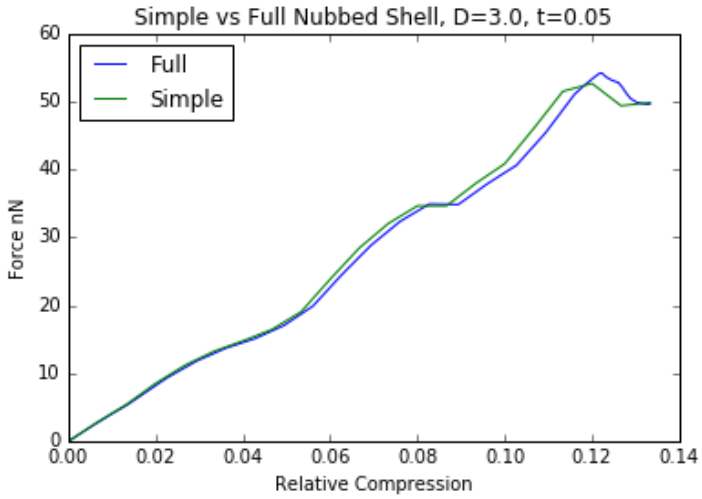

Figure 3.18: Simplified model and full model $F-\Delta$ curve.

3.17a. Reissner, covered earlier predicts that shells strain is negligible once you get a certain distance from the point of contact. This indicates that the simplified model is a valid assumption for the initial region of the simulation. The simulated $F-\Delta$ curve of both the full and simplified model is shown in Figure 3.18.

Calibration of Simplified Shell

The simplified shell section should ideally behave exactly as the nubbed section. A reasonable approximation was made by comparing two square sections with identical BCs. A 1x1x0.05 plate was created with and without small spheres. All DOFs were disabled on one

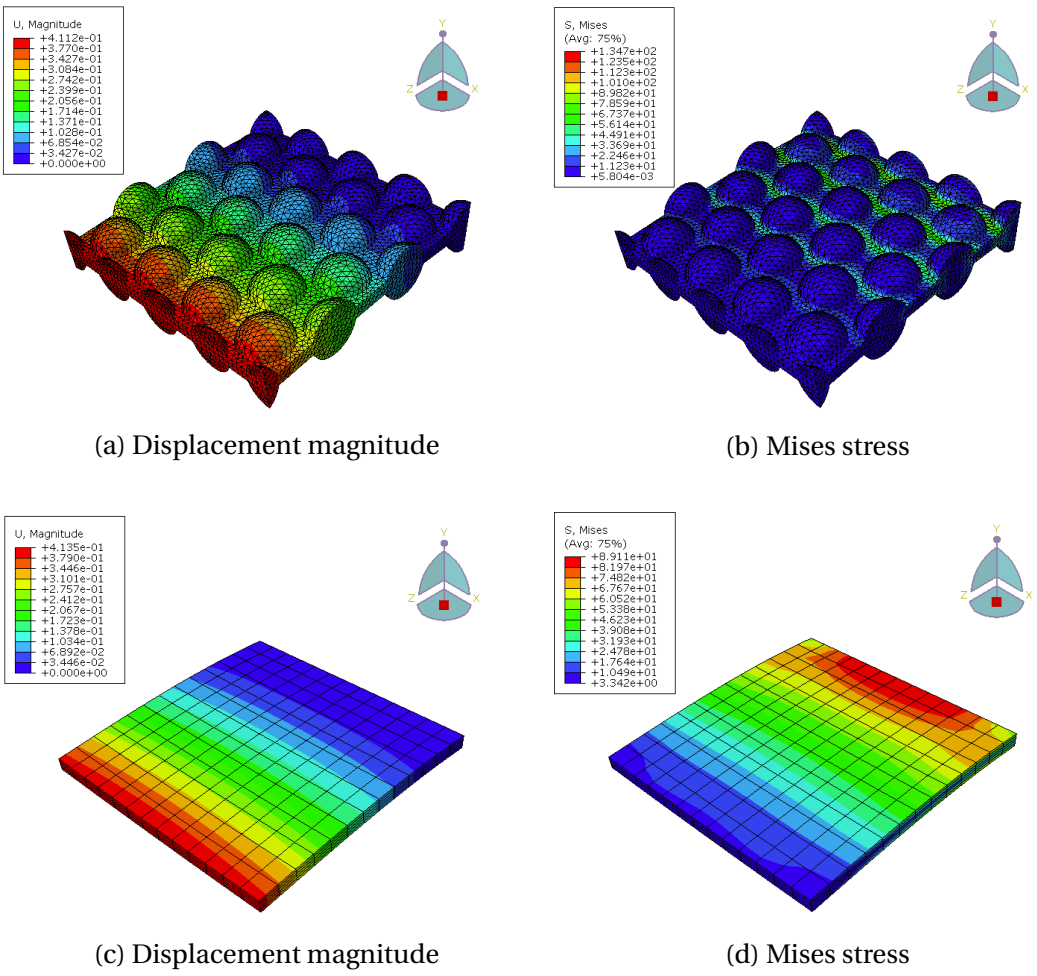

(a) Displacement magnitude

(b) Mises stress

(c) Displacement magnitude

(d) Mises stress

Figure 3.19: Comparison of a nubbed and simple calibration plate.

side while a shear force was applied to an identical cross section on the opposite side. The elastic moduli of the simple plate was adjusted until the maximum displacement for the two models was similar, see Figure 3.19. The model shows a stiffness ratio of about 1:3.5 between the nubbed and simple plate. This ration was used in the subsequent models to get a representable response from the simpler shell. Depending on the geometry this simplifications reduces the number of elements by 3/4 something which drastically reduces computational cost. This simplified model was only used with the HILE material model as the stiffness of the model scales approximately linear. Depending on how the input variables are adjusted this is not the case for the Yeoh material.

Mesh and Element Properties

The simplified model employs the full tetrahedral mesh (C3D10) for the upper eighth of the sphere. The lower simple geometry was meshed with three or four hexahedral (C3D20) ele-

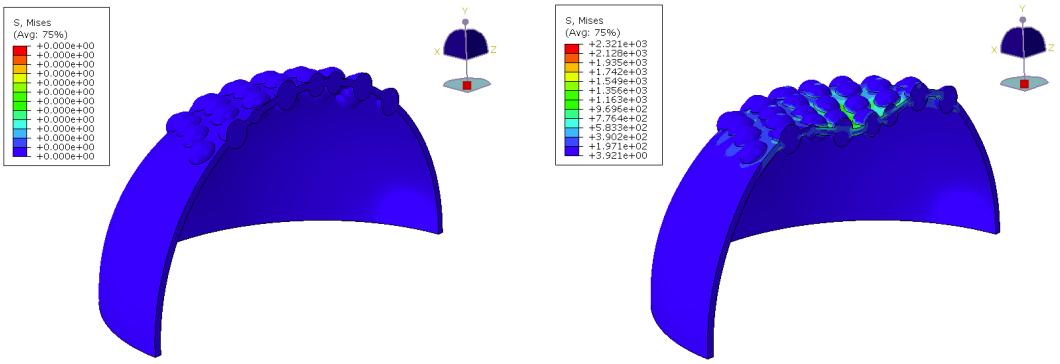

(a) Undeformed simple NP-MB (b) Deformed simple NP-MB

Figure 3.20: Deformation geometry of simplified shell

ments across the thickness with large second and third dimension. The boundary between the sections requires incompatible elements as they have a different number of nodes. Due to the incompatible elements not being located in a large strain portion of the model it is assumed that their behavior does not introduce any significant error.

Deformation Geometry

The deformation geometry of the simplified shell is shown in Figure 3.20.

3.6 Sensitivity Study

To get an idea about how the model responds to uncertainties in the input variables we ran a spectrum of simulations across relevant parameters for the HILE material model. These parameters include the diameter, shell thickness, NP diameter and NP packing. Previous simulations have also also run in order to justify the assumed boundary conditions, for example ignoring the effect of any internal gas or the effect of contact friction.

A general comment can be made about the steps seen in the $F-\Delta$ curves. These are presumably caused by new NPs coming in contact with the compressing plate. This temporary alters the stiffness and will in the later regions of the compression contribute to the buckling of the shell.

3.6.1 Diameter

The simulations $F-\Delta$ curves are shown in Figure 3.21. These simulations all have a shell thickness of 50nm and a packing density, Q, of 60. The HILE material has a Young's modulus

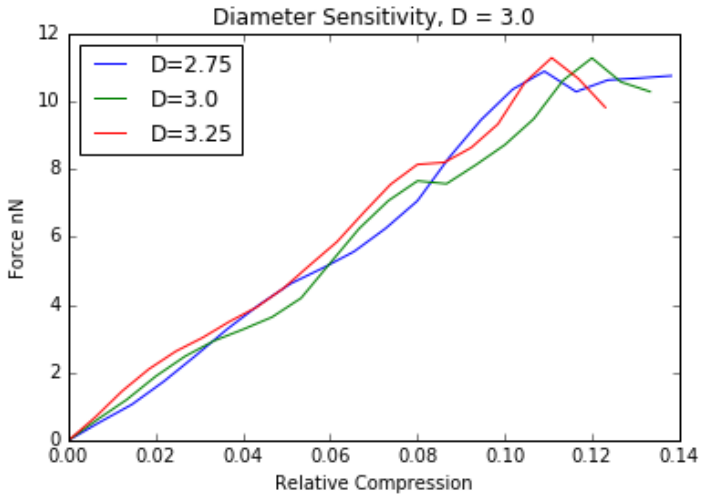

Figure 3.21: $F-\Delta$ curve of various diameters.

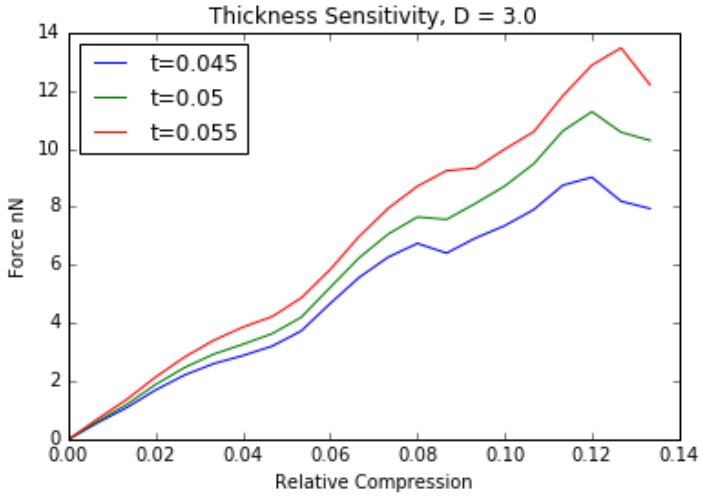

Figure 3.22: $F-\Delta$ curve of various thicknesses.

of 30 MPa. The diameter is a highly relevant parameter as the accuracy of the tested MB diameter is poor. The plot shows that the diameter does not significantly affect the resulting force. The oscillations are attributed to a different contact sequence for the NPs, as they are distributed slightly different for each diameter.

3.6.2 Shell Thickness

The simulations $F-\Delta$ curves with various thicknesses are shown in Figure 3.22. There is a significant effect on the MB stiffness as various thicknesses are simulated. This indicates the importance of the parameter. NPs are located identical for the different thicknesses which contributes to the similar oscillating behaviour.

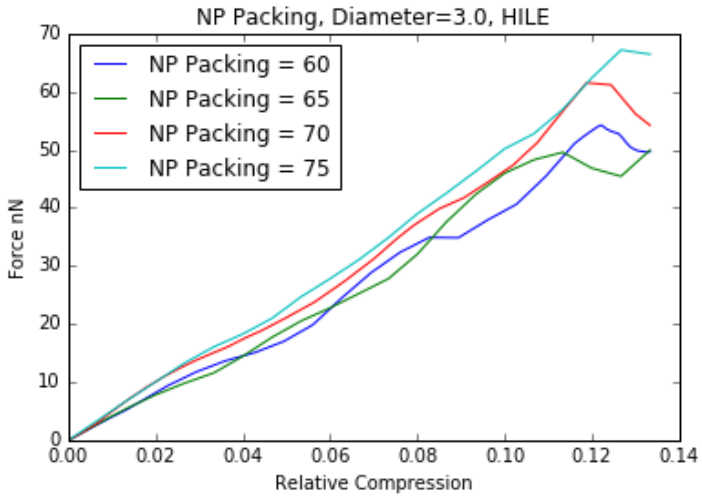

Figure 3.23: $F-\Delta$ curve of various thicknesses.

3.6.3 NP Density

The packing density of the NPs seem to primarily affect the initial oscillating behaviour. The oscilation of the $F-\Delta$ curve is attributed to when new NPs come in contact with the compressing plate. This becomes less evident as NP packing increases due to the increased stability and stiffness caused by inter NP bending having to occur on a smaller area of the MB shell.

3.6.4 NP Diameter

A limited number of NP diameters were simulated and is presented in Figure 3.24. It appears that the $F-\Delta$ curves oscillation is largely dependent on the NP packing where smaller NP-MB simulations exhibit a similar but softer behaviour when the packing density is kept constant.

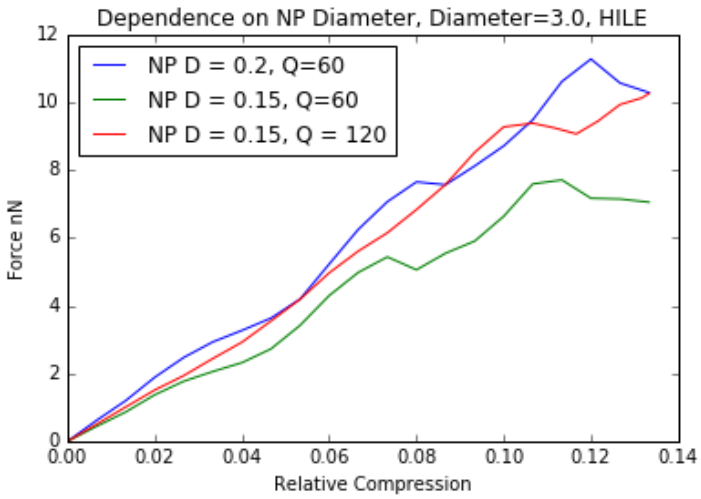

Figure 3.24: $F - \Delta$ curve of two different NP diameters and two different packing densities.

Chapter 4

Results

4.1 Infer Shell Thickness from Buckling Point

4.1.1 Data Insight

Finnøy's $F - \Delta$ curves have a reoccurring plateau. In order to check potential insights we define the buckling to be at the inflection point of the first drastically reduced slope. In most cases this would be where the slope is either close to or lower than zero. By employing this criteria on Finnøy's graphs from 2013 (Appendix A) we can identify a decrease in buckling point as a function of diameter. All available data points were plotted in Figure 4.1. There seems to be a negative dependence on the diameter. Unfortunately the sample size is not large enough to conclude if the relation between the buckling point and the NP-MB diameter is either linear or exponentially decaying. This same plateau is not evident in the limited data available from Moe's experiment, due to the low maximal load.

The simulations also exhibit a buckling behaviour. When using the HILE material the buckling point is not dependent on the material stiffness. This means the force in Figure 4.2a and 4.3a can be normalized.

To estimate the shell thickness we first establish the buckling point for the AFM data. By finding diameter and corresponding buckling point in Figure 4.2, the remaining difference is found in Figure 4.3 and then used to predict the shell thickness. The relation between the NP diameter and NP packing density is complex. This method was not the primary focus of the thesis and the limited resources allocated means the complex relations were not adequately described. A linear perturbation buckling analysis of a point load failed to yield predict the

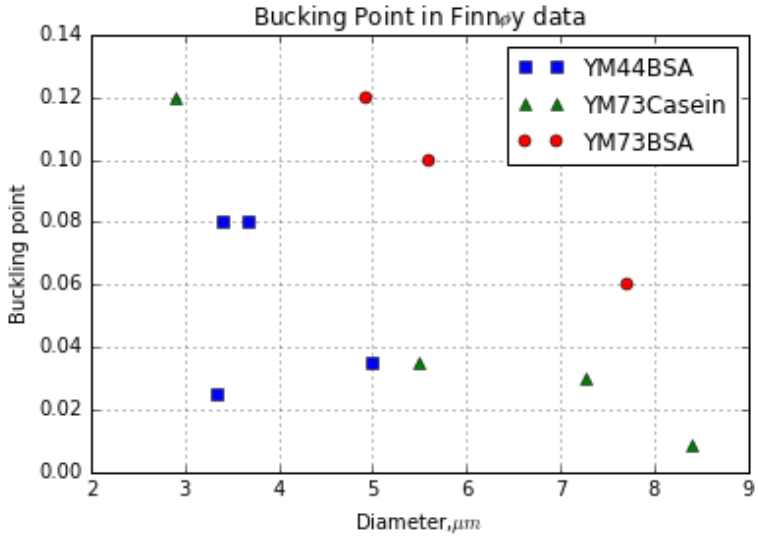

Figure 4.1: Buckle point in Finnøy's data, See appendix A

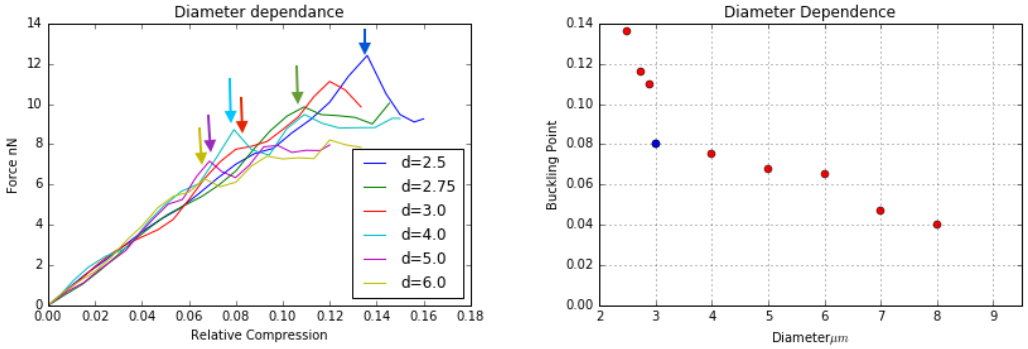

(a) (b)

Figure 4.2: (a) $F-\Delta$ curves of different diameters. Not all plots are included. (b) The simulated buckling point plotted as a function of diameter, $t = 0.05\mu m$.

observed buckling point and is therefore not included.

An alternative way of determining the shell thickness was also presented by Lytra et al. [23]. Using polymeric and lipid MBs they employ a combination of the Reissner Theory [18, 19] for the initial linear region and the Pogorelov model[57] for subsequent buckled state to estimate both the Youngs modulus and the thickness. This has not been applied to Moe or Finnøy's data as it considers a smooth sphere. The method presented here is similar to the one in Lytra et al. as it not only considers the transition to the buckled state but also includes the geometric effect the NPs contribute. The estimated shell thicknesses are presented in Figure 4.5. The lowest buckling values were not possible to estimate based on the simulation data at hand. This could indicate indicates that the excluded factors are of importance or that the data from the simulations is wrong and not applicable. The only discernible trend is

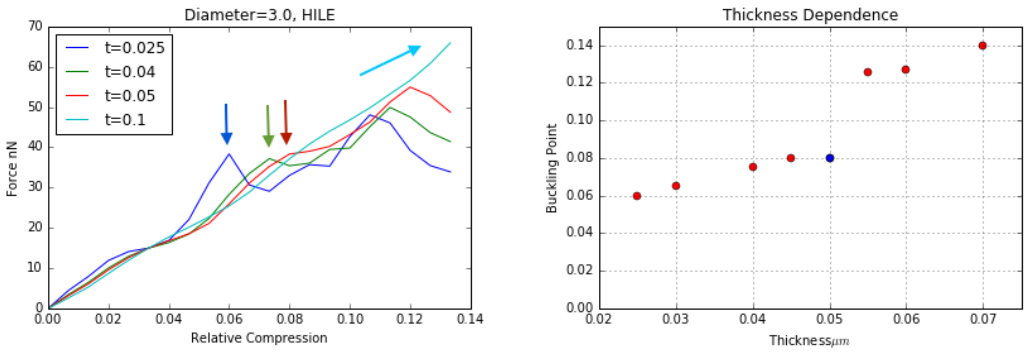

(a) (b)

Figure 4.3: (a) $F-\Delta$ curves are scaled to an equal force at $\epsilon_{Def} = 0.035$, not all plots are included. (b) The simulated buckling point plotted as a function of thickness, $D = 3.0\mu m$.

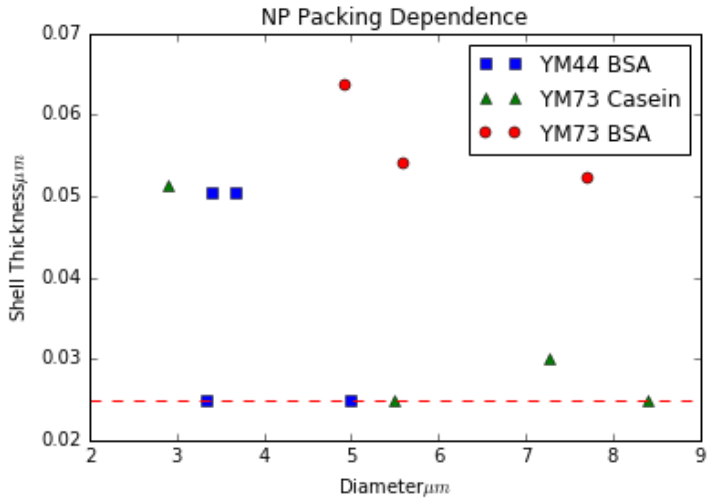

Figure 4.4

Figure 4.5: Finnøu's data with estimated thickness as a function of diameter. Points on the red dotted line are not properly estimated as their response indicated an even thinner shell than the simulation data can estimate.

for the YM73BSA where there seems to be a negative correlation with the diameter.

4.2 Simulation Compared to Experimental Data

The two different material models presented in chapter 3 were run on the nubbed sphere geometry. Figure 4.6 illustrated the different stress and strain response of the two materials. The strain in the HILE model is localized close to the loading area, illustrated in Figure 4.6a. The very low linear stiffness coefficient means significant deformations also occur far from the loading area. This means that we will see a later buckling response as the supporting part

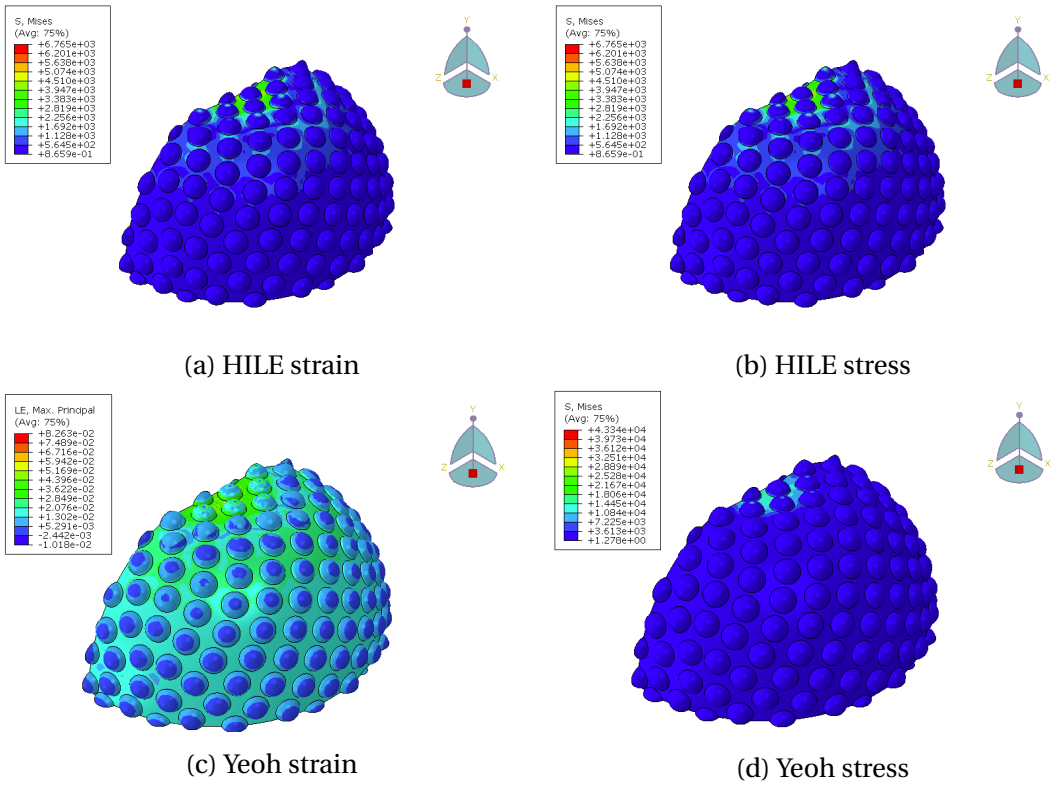

(a) HILE strain

(b) HILE stress

(c) Yeoh strain

(d) Yeoh stress

Figure 4.6: Stress and strain comparison of the HILE and Yeoh material models for the GB167 Nr13 MB

of the sphere also deforms. This is illustrated in Figure 4.6c where the majority of the strain seen in the shell is of the same order of magnitude. This is in strong contrast to the HILE model where large localized strains contribute to most of the deformation. The uniform distribution of strain in the Yeoh model means that larger deformations will also occur at the NP locations.

4.2.1 HILE Material

The Young's modulus of the simulation data was adjusted so that the maximum force and displacement of both the simulation and experiment coincide. This method of fitting the Young's modulus will also underestimate the stiffness towards the end of the data if we assume a constant slope for a hypothetical continued loading. As can be seen from Figure 4.7 we were not able to reproduce the initial non-linear region with the HILE material. This mismatch is also seen with the GB161 experimental data. The Young's modulus' calculated from the available data is plotted in Figure 4.8. The there is no evident dependence on the diameter and the difference in Young's modulus for similar diameter MBs is large. This method of

determining the Young's modulus is therefore not a good alternative.

4.2.2 Yeoh Material Model

The Yeoh models exhibits a non-linear behaviour and yields a better fit to the experimental data. Figure 4.11 shows GB167 bubbles plotted against simulation data. The coefficients used for both the GB161 and GB167 batch are presented in table 4.9. The experimental data's tendency to exhibit a rapid increase in stiffness followed by a region of constant stiffness is not explained by the Yeoh parameters used. Unfortunately it was not possible to run a full array of parameters due to this material being included at a late stage of the project. Similar to the tensile stiffness of the HILE model, there is a large span in the coefficients. The average of the GB167 fitted C20 parameter was used on a standard bubble $D_{MB} = 3.0\mu m$. This is plotted against the 40nN experimental data from Moe in Figure 4.10.

The sensitivity study covered in the simulation chapter was done with a HILE material. Due to uncertainties about the assumed packing density a comparative simulation was also run with the Yeoh material. This is shown in Figure 4.13.

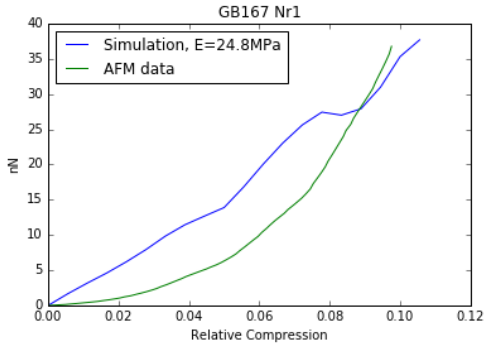

(a) Nr 1

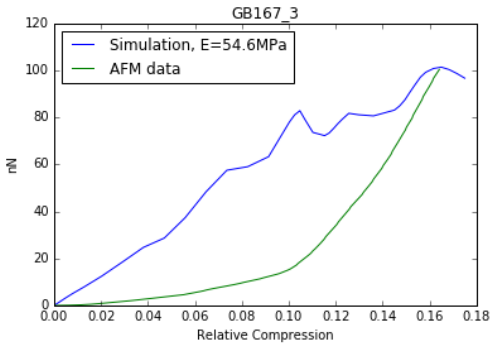

(b) Nr 3

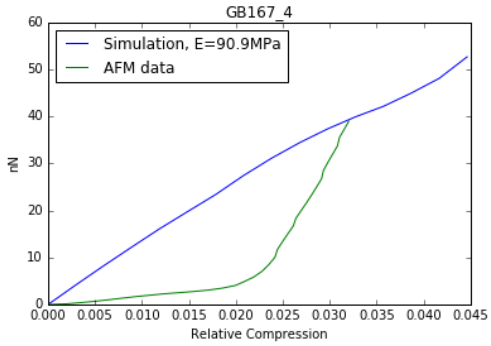

(c) Nr 4

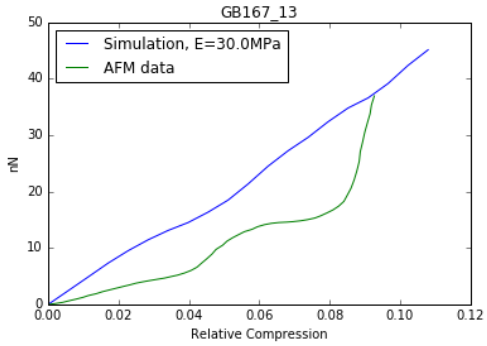

(d) Nr 13

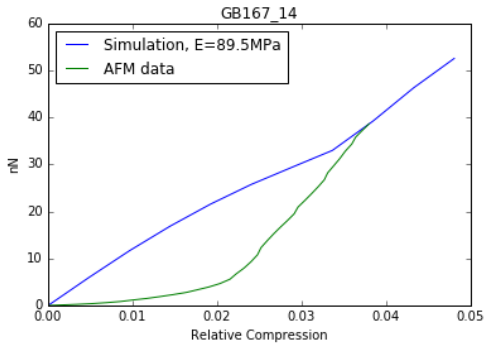

(e) Nr 14

Figure 4.7: HILE simulations visually fitted to the GB167 experimental data.

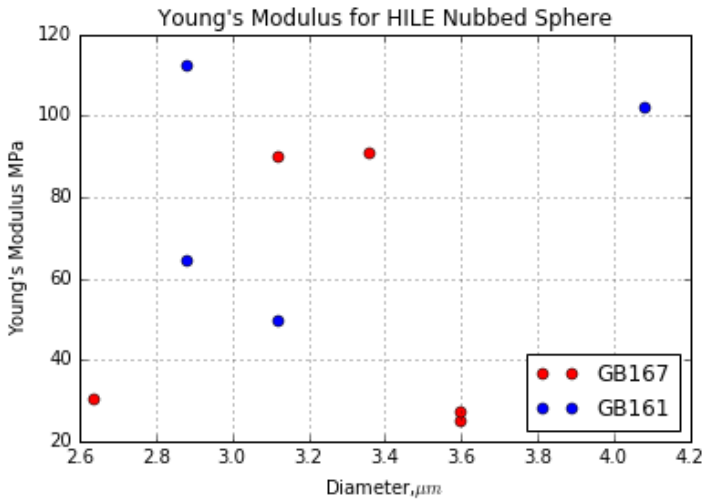

Figure 4.8: GB 167, Young's Modulus as a function of diameter.

Bubble	C10	C20	C30
GB167 Nr 1	100	$1.84 \cdot 10^6$	0
GB167 Nr 3	100	$0,96 \cdot 10^6$	0
GB167 Nr 4	100	$32.0 \cdot 10^6$	0
GB167 Nr 13	100	$2.04 \cdot 10^6$	0
GB161 Nr 1	100	$5.32 \cdot 10^6$	0
GB161 Nr 2	100	$120 \cdot 10^6$	0
GB161 Nr 4	100	$13.1 \cdot 10^6$	0
GB161 Nr 6	100	$30.6 \cdot 10^6$	0

Figure 4.9: Yeoh parameters fitted by visual inspection.

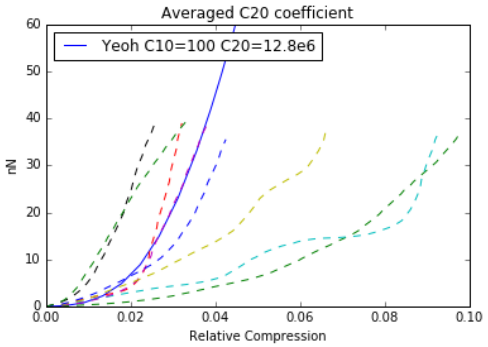

Figure 4.10: Simulation run with the C20 coefficient averaged across the GB167 simulations and plotted against all 40nN $F - \Delta$ curves.

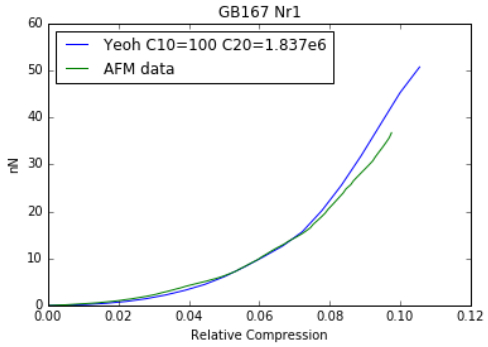

(a) Nr 1

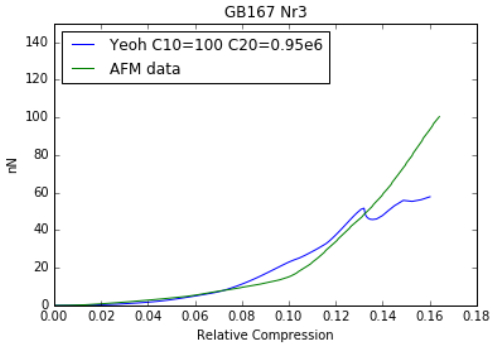

(b) Nr 3

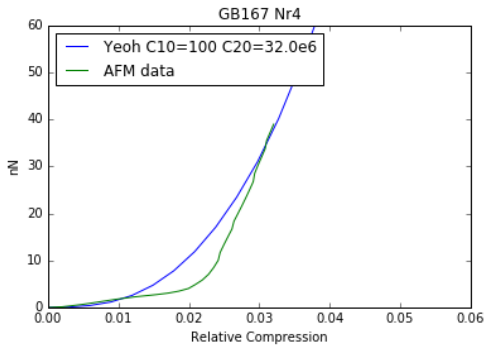

(c) Nr 4

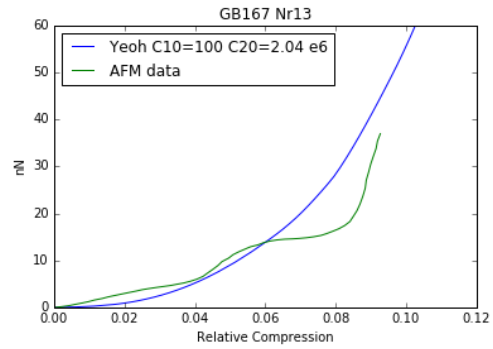

(d) Nr 13

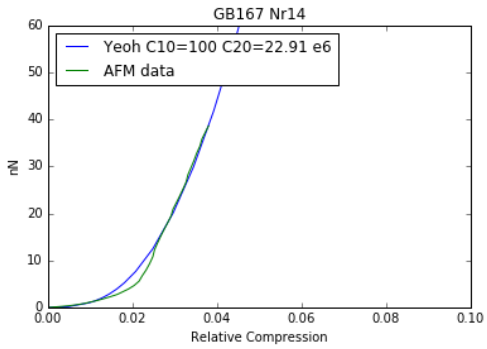

(e) Nr 14

Figure 4.11: GB 167 bubbles compared to Yeoh simulation data

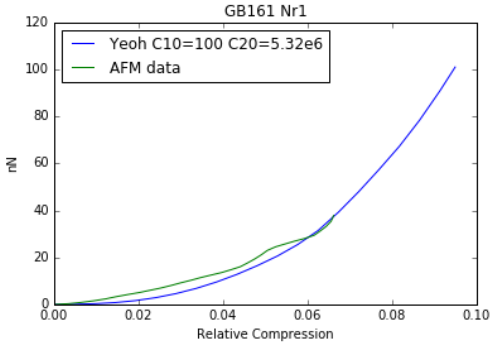

(a) Nr 1

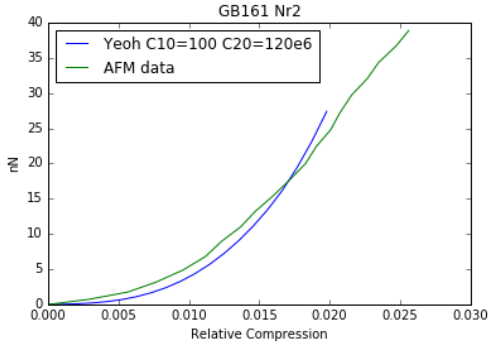

(b) Nr 2

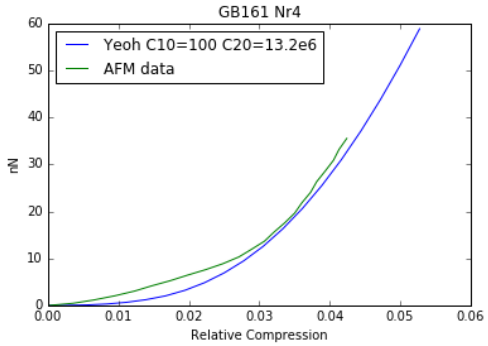

(c) Nr 4

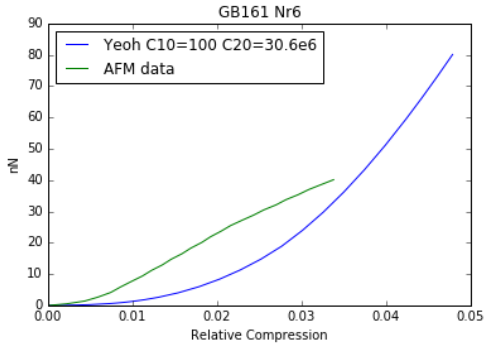

(d) Nr 6

Figure 4.12: GB 161 bubbles compared to Yeoh simulation data

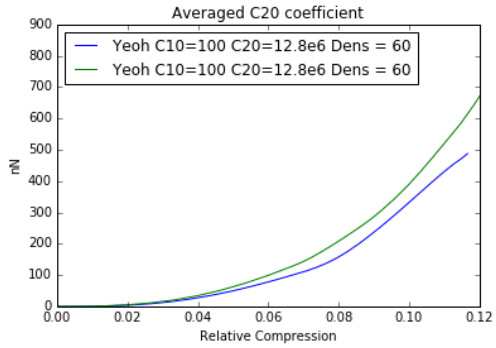

(a)

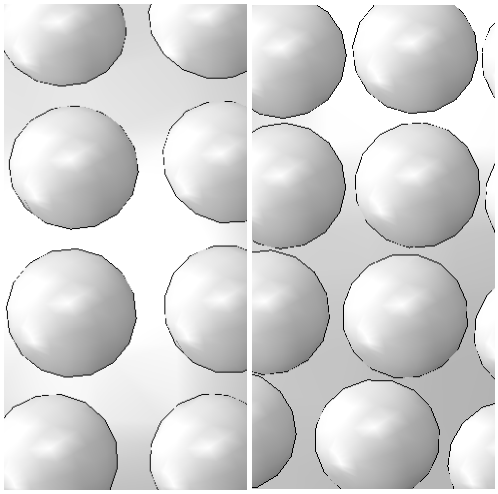

(b) (c)

Figure 4.13: (a) $F-\Delta$ curve of the two packing densities. (b ,c) Illustrates the modeled surface geometry of packing density $Q = 60$ and $Q = 75$.

4.3 Reissner Theory vs Simulation

As seen in all the experimental $F-\Delta$ curves the initial slope is zero. This comes from the definition of contact as covered in Section 2.3.1. As discussed previously this is is attributed to unknown boundary conditions or material non-linearity. Comparing the simulation data to the Reissner theory we can see that it could be used as a reasonable estimate for the parallel plate compression of both a perfectly smooth sphere and the nubbed sphere.

4.3.1 Smooth Shell

The Reissner Theory is shown to be a reasonable estimate for the initial deformation regime. Figure 4.14 compares the Reissner Theory to two different shell thicknesses with a diameter $D = 3.0$. There is some mismatch in the initial stiffness, something that might be due to a contact coarser mesh in the thicker shell. The Reissner Theory seems to be a good estimate up to a relative compression $\epsilon_{Def} < 0.05$.

4.3.2 Nubbed Shell

As seen in Figure 4.15 the Reissner theory yields a reasonable estimate for relative deformations smaller that the buckling point, typically $\epsilon_{Def} < 0.05$.

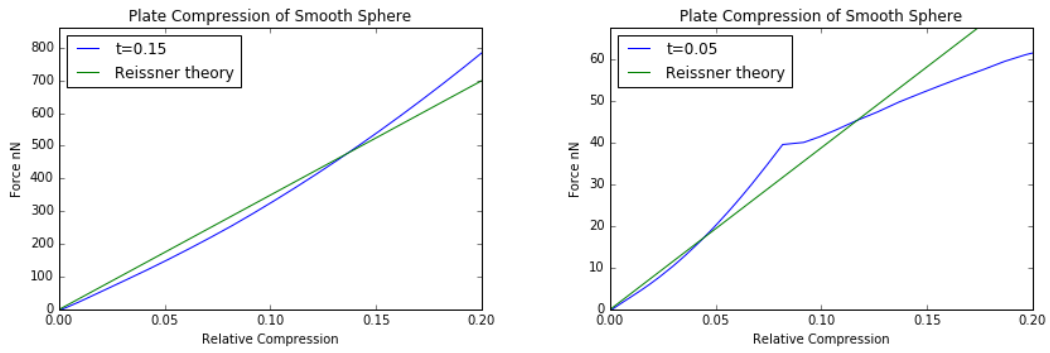

(a) (b)

Figure 4.14: Plate compression of a smooth shell compared with the linear Reissner Theory.

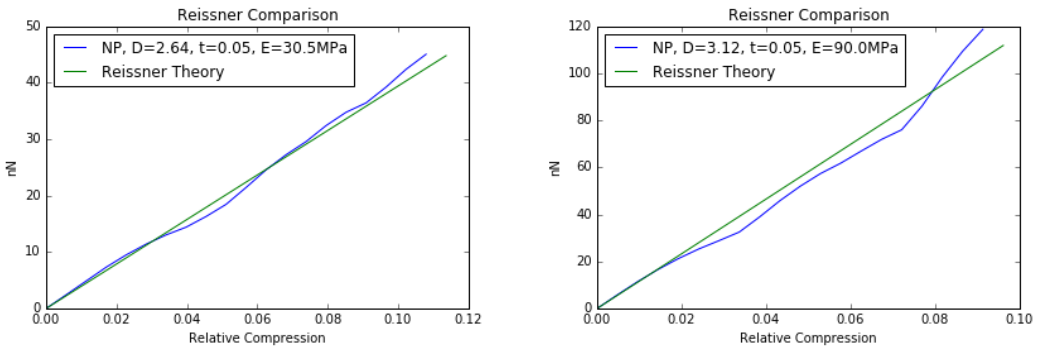

(a) (b)

Figure 4.15: Plate compression of a nubbed shell compared with the linear Reissner Theory.

4.4 Viscoelasticity of Shell

When looking at both the approach and retract $F-\Delta$ curve of each individual bubble, about half of them exhibit a notable hysteresis. Due to the hysteresis only being present after cantilever bending is initiated, we can assume that the hysteresis is not induced by viscous drag as the cantilever moves through the water. This leaves the shell material as one potential cause of the hysteresis. To estimate the viscosity we will assume that the rate of loading is the same in both directions due to the contrary not having been explicitly stated. The scan rate of the AFM is covered in Section 2.2. We can then establish an average force which will give us the magnitude in force being induced by viscous resistance. As stated in Chapter 2 the resulting average is not suitable for shell stiffness estimation. This is due to effects like tip binding which causes an upwards force on the bubble as the cantilever retracts past the initial contact point. The rate of bubble compression is different from the scan rate. As the cantilever touches the bubble it will deflect and the effective rate of the bubble compression is reduced. By finding the rate of compression of the bubble we can determine the viscosity of the bubble. In order to obtain the viscosity of the shell we have to relate the bubble viscosity to the deformation geometry of the shell. The finite deformation of an elastic MB shell will have the same deformation geometry as a quasi-static loading of a viscoelastic MB shell. Assuming the deformations of a viscoelastic MB happens in a similar fashion for both dynamic and quasi-static loading we can relate the shear strain to the rate of strain. The shear strain rate $\dot{\gamma}$ is assumed to be proportional with the relative compression rate $\frac{\dot{u}}{D_0}$ and hence the shear modulus being proportional to the shear viscosity. The shear modulus is given by $G = E/2(1+\nu)$. Employing these assumption to the Reissner Theory equation (4.1), we ob-

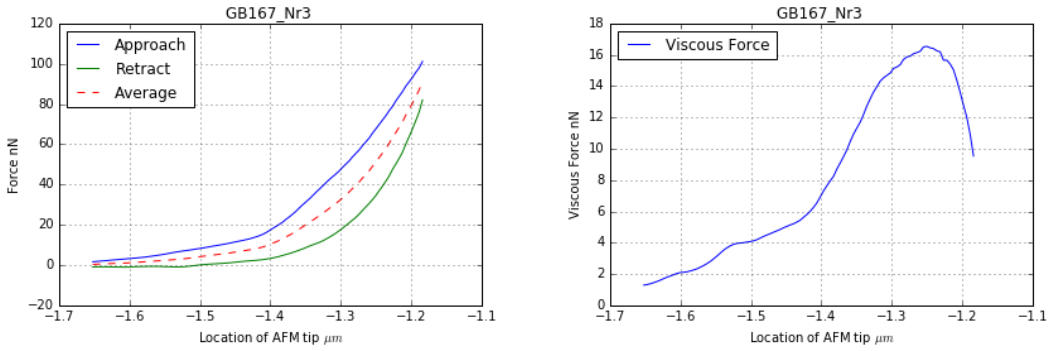

(a) (b)

Figure 4.16: (a) The $F-\Delta$ curve of both the loading and unloading is plotted with the average of the two. (b) Viscous resistance as a function of displacement.

tain a new equation for the viscous contribution to the force equation (4.3). Rearranging this equation we can obtain an estimate for the viscosity of the material with (4.4). A Poisson ration, $nu = 0.45$ and a constant shell thickness was used. The maximum value of the viscous contribution was used to compute the viscosity. The estimated viscosity is presented in Figure 4.17

$$F = E\frac{4}{\sqrt{3(1-\nu^2)}}\frac{t^2}{D_0}u \tag{4.1}$$

$$F = 2G(1+\nu)\frac{4}{\sqrt{3(1-\nu^2)}}\frac{t^2}{D_0}u \tag{4.2}$$

$$F_{visc} = \mu\frac{8(1+\nu)}{\sqrt{3(1-\nu^2)}}\frac{t^2}{D_0}\dot{u} \tag{4.3}$$

$$\mu_s = \frac{\sqrt{3(1-\nu^2)}}{8(1+\nu)}\frac{D_0}{t^2}\frac{F_{visc}}{\dot{u}} \tag{4.4}$$

This result is vastly different from the Finnøy data where casein MB viscosity was determined by theoretical attenuation estimates and parameter fitting ($\mu_s = 1.29\pm 0.06$ Pa s). The thickness assumed by Finnøy was $0.15\mu m$ as opposed to our $0.05\mu m$ but even when employing our simple consideration with Finnøy's assumed thickness, the viscosity is still three orders of magnitude larger ($1.9\cdot 10^3 Pas - 136.8\cdot 10^3 Pas$). This discrepancy raises large concerns about the validity of this simple consideration and this method is probably wrong.

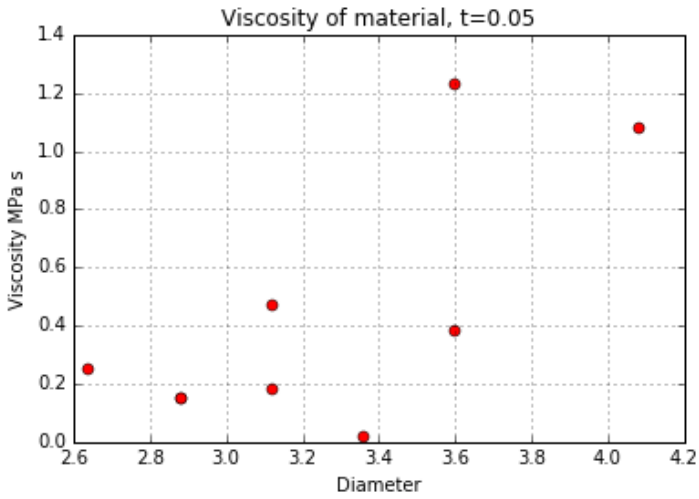

Figure 4.17: The viscosity if the shell was estimated with a constant thickness of 0.05μm across the datasets.

Chapter 5

Discussion

5.1 Experimental Data

The limited data set available is one of the biggest challenges faced in this thesis. A larger number of data sets would help us distinctly isolate phenomenons seen in the $F-\Delta$ curves. Right now we have no way of determining if an observed effect is unique or part of other data sets exhibiting the same behaviour. For the available experimental data there seems to be a trend of "soft" and "firm" bubbles. The stiff bubbles all undergo a relatively small relative compression where an initial softer region is followed by a sharp increase in stiffness. The later parts of the "stiff" $F-\Delta$ curve appear linear. The softer bubbles seem to all display some form of non-linearity across the entire deformation regime. There is no correlation between the stiffness and batch or diameter. Based on the data from Moe and our FEM simulations it is still not possible to determine if the non-linearity is caused by material specific properties or other external unknown boundary conditions. A larger sample size, including larger deformations, might allow us to distinctly discern trends and anomalies which could reduce the apparent lack of correlation in the experimental data.

5.1.1 Contact Point

The contact point definition will impact how much of the initial non-linear region will be included in the $F-\Delta$ curve. Our chosen approach to determining the contact point is conservative as it includes all initial contact effects. The manual approach of the direct analysis in our definition would be problematic for a larger sample size. A simple algorithm for defining the required parameters could be implemented in order to manage a larger data set. This

definition is in contrast to Finnøy's approach which defined the contact point as where the magnitude of the slope was above a certain value. This strict metric which purposely excludes some of the small slope found in the initial region. The size of the excluded regions in the Finnøy's data is not known.

The variety of definitions of contact points in other studies creates difficulties in comparing both experimental and simulation $F-\Delta$ curves with other external analyses and data. This is an issue when attempting to predict a shell thickness for the Finnøy data as he has employed a strict metric for contact point which purposely eliminates small initial slopes (see Section 2.3.1).

5.1.2 Diameter of bubble

Due to the limited resolution of the AFM imaging equipment, the diameter of individual bubbles can not be accurately determined. The pixel size in the tested bubble images equates to $0.24\mu m$. As seen in the sensitivity study for the HILE material, this diameter uncertainty is not detrimental for the estimated stiffness. The sensitivity study indicates a fluctuating error up to around 10%. The oscillations are probably caused by a different NP packing structure as the NPs are uniquely placed for each diameter. This error is not considered critical due to the span of tensile modulus being orders of magnitude larger than the potential error caused by the diameter uncertainty. A. Bjørkøy (Department of Physics) since obtained a new imaging system with a maximum resolution of 150nm. This will improve the accuracy of the reported diameter for future experiments.

5.1.3 Stiff vs Soft Bubbles

As mentioned previously the $F-\Delta$ curves can potentially be grouped into two categories: stiff and soft. This is can be seen in Figure 2.11. It is possible that the bubbles with a stiffer $F-\Delta$ curve was deemed undeformed. It might be hard to observe a perfect depression of the center of the MB as the thickness of MB that creates the image contrast would remain the same. Glynos et al.[20] observed permanent deformations polymer MBs was possible. Due to the limited data, it is not possible to suggest a permanent deformation as the cause of the stiffer bubbles.

Looking at all of Moe's data, the curves seem to have a similar stiffness towards the end of the compression. This was investigated further and a seemingly linear relation between

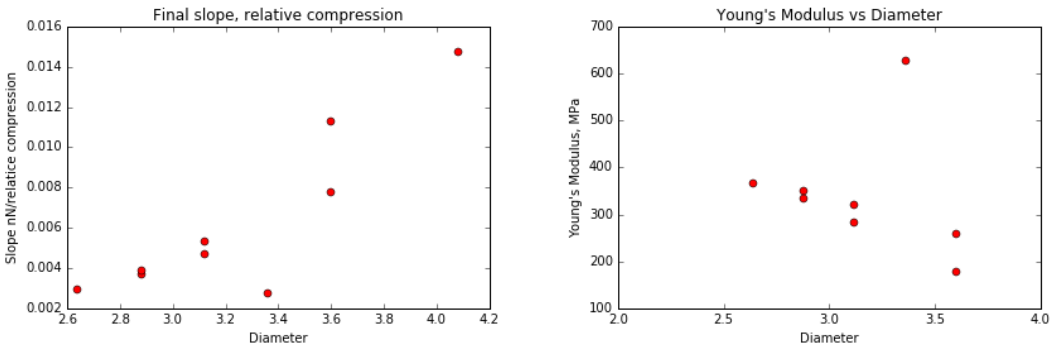

(a) (b)

Figure 5.1: (a) Slope of last five data points for each GB MB. (b) Young's modulus corresponding to the later part of the experimental data.

bubble stiffness and diameter is seen. This evaluation was done by calculating the slope between data point N and N-4. The resulting stiffness is shown in Figure 5.1a. We can create an alternative estimate for the Young's modulus of a HILE NP-MB by assuming that the initial non-linear regime is caused by external BCs and not pure deformation of the bubble. This is alternative representative region also assumes that initial non-linear effects can not be attributed to material non-linearity. By looking at the later region of compression the undetermined BCs can be considered displaced or otherwise negligible. Based on the Reissner theory being a good assumption for the initial compression of a perfect HILE NP-MB, we can obtain an alternative Young's modulus from the calculated stiffness. A constant thickness of 50nm was used and the resulting Young's modulus is shown in Figure 5.1b.

An experimental specific uncertainty is the challenge of centering the AFM cantilever over the NP-MBs. This might also cause errors in the reported $F-\Delta$ curves. Any non-center loading could potentially cause the cantilever to twist, something that would negatively impact the accuracy of the force measurement.

5.1.4 Initial Non-linear Behaviour

Based on the information gathered and simulations run, it appears that the non-linear region is attributed to either a non-linear material model or other still undefined boundary conditions. As seen by the simulations employing the HILE material model, the non-linear region has no apparent geometric explanation. Any linear material will have an initial stiffness where as the experimental data has no initial stiffness. The Yeoh material model better represents this effect. Setting the C10 coefficient to 0 or close to zero we are able to obtain

a very soft initial response. The Yeoh simulations corresponds better to the experimental data. A potential material non-linearity is supported by the typical non-linear $\sigma - \epsilon$ curve of protein. This alone is not enough to support this as the single determining cause of the initial non-linearity. Boundary conditions that can induce non-linearity are for example PEG-chains on the outside of the NPs. Their length and density is scarcely documented and the displacement of a grass-like structure could have a greater influence on the $F - \Delta$ curve than originally reasoned in Section 2.1.3. The effect of the entire NP-MB being coated in a layer of protein might also influence the initial contact behaviour. There could also be an undocumented electrostatic repulsion between the MB and the cantilever tip. The Coulomb charge, C, required for two charged points 5nm apart repelling each other with 5nN would require 3.7C. This equates to about 3 Ampere seconds. It is not known if such a charge could persist for both the tip and the coated dish. The Yeoh form used in our simulations behave similarly with an exponential $\sigma - \epsilon$ relation and seems to fit the experimental data much better than the HILE material model. Another non-linear effect might be the solubility of the casein used in the GB batch. A hydrated outer layer of casein or HSA[34] might provide some initial resistance, seen in the $F - \Delta$ curves. Due to the number of different models of casein it is difficult to draw insight from its properties [58] and it was neglected.

The $F-\Delta$ curves were calibrated with a sensitivity study which showed a short initial non-linear response. The glass base subject to the sensitivity study is coated with a polymer which could contribute to this. It is not known of the sensitivity study was done on the same glass base as the bubble compression. Different polymer thicknesses both globaly and regionaly on the glass base would impact the non-linear influence on the bubble measurements.

5.2 Shell Properties

The MBs estimated Young's modulus for the HILE simulations range from 24.8-112.5 MPa and there was no obvious correlation to the diameter. The method of fitting the $F - \Delta$ curves is highly subjective. Without making unjust assumptions about the initial non-linear region, it is not possible to get a good prediction of the MBs tensile modulus using the HILE material. The Yeoh model was used with a low initial stiffness, $C_{10} = 100$, and the resulting C_{20} parameters ranged from $0.96e6 - 40e6$. The Yeoh model was fitted visually with one iteration. The C_{30} parameter was set to 0 for all experimental fittings as involving this parameter would

have complicated the fitting process further. In hindsight this variable could better describe the sharper rise in stiffness seen in the "stiff" bubbles. An alternative fitting method could have incorporated a matrix of variables dependent on a cost function. The cost function is dependent on the simulations deviation from the experimental data and minimizing this would optimize the coefficients. This method would require a refined model as the simulation time associated with this iterative approach would be large.

Both material models have also been assumed isotropic and homogeneous. This is a very big leap to take for example due to the dimensions of the shell thickness possibly being less than 5-10 molecules. Presently, no information has been found about the validity of continuum theory for protein deformation on this scale. Being able to describe the thickness in integer multiples of molecules strongly indicates that continuum theory could very easily fail.

Taking the GB167 Nr 13 MB as an example, we can look at the reasonableness of the resulting stresses. The HILE model has a final maximum Mises stress of around 6.7 MPa where as the Yeoh model has a final maximum Mises of 43 MPa. This large difference is attributed to the Yeoh models smaller contact area, illustrated in Figure 4.6c, causing higher localizes stress. A study investigated a casein and glycerin(70%/30%) film which was shown to exhibit tensile modulus of between 1 and 15 MPa[59]. The thickness, $20-180\mu m$, was significantly larger than what is found in the MBs. This creates uncertainty about this estimates applicability. This experiment was conducted in air meaning there is no liquid interface. It was found that the modulus was negatively correlated to the air humidity, which further dissuades comparison. This experiment is not directly comparable and does not directly invalidate the much higher tensile modulus seen in the MB experiment. Looking at the available material properties of HSA, assumed to be similar to BSA, we see that our Young's modulus estimate is similar to the minimum breaking strength of HSA. HSA's secondary structure is approximately $4x4x14nm$ in size [60] and an individual HSA molecule is stronger than the reported unbinding force between the HSA and HSA antibody. The breaking strength of 90-244pN[48, 61] translates to a breaking stress $\sigma_{/break} < 5.6-15.5MPa$. A layered protein structure would probably exhibit a higher breaking due to it being held in place along it's length as opposed to only being fixed at the ends. The studies only mentioned the breaking strength and it is therefore not possible to say anything about the tensile modulus. If we look at the different proteins as whole, our simulation data are within the same order of magni-

tude as a proteins breaking strength. Further literature about the breaking strength or tensile modulus of casein or BSA was not found.

5.2.1 Constant Thickness vs Constant Tensile Modulus

Due to the difficulty of determining the shell thickness of the MBs it is often presumed constant. This might not be the most sensible approach considering that materials of similar composition should exhibit similar material properties. This is not the case for the tensile modulus estimates seen in this thesis. The largest estimate for the Young's modulus is a factor of four larger than the smallest. The same trend is seen with the Yeoh model. The large spread in the experimental data is not even close to a single material parameter. This is something that indicates other factors, like the shell thickness playing an important role in the MB behaviour.

5.2.2 Estimating Shell Thickness

Our method of estimating the shell thickness as a function of buckling point show that the shell thickness might be negatively related to both MB diameter and shell thickness. The steps present in the buckling dependence plots are attributed to the geometric effect of the NPs. Previously Lytra et al.[23] has employed a theoretical pre- and post-buckling of perfect spheres in order estimate the stiffness and shell thickness. This method is not applicable to our MBs primarily due to a different loading condition.

As seen in the estimated thickness plot, we hit a lower threshold for the thickness. This is due to not having simulated thinner shells, thus not having any data to interpolate. The thinner shell was not modeled due to the thinner shell still requiring a minimum number of nodes across the thickness. This is something which drastically increases the number of elements required, driving the computational cost up. A thinner models should be investigated further in order to be able to estimate the shell thickness of the MBs with a low bucking point. Presently only the shell thickness and MB diameter is included. The effect of packing density is shown but not included in the estimates. As seen in the sensitivity study, the response is also dependent on NP diameter, contact friction and NP location relative to the initial contact point. The effect of these were not investigated so their effect is difficult to quantify. The estimation of the Finnøy MBs buckling point was also done by direct analysis and is therefore highly subjective. An algorithmic approach to determining the buckling

point should be developed. It's application requires numerical data, something that was not available for the Finnøy data. Again, in hindsight, the Yeoh material model should have been run for this experiment too. The large displacement response look similar to the HILE model except that the pre-buckling stiffness is maintained.

5.3 Simulated MBs

5.3.1 Smooth Shell

The plate compression of a smooth shell did not provide much insight into the NP-MB behaviour. The initial linear region indicates that the Reissner Theory could be a good estimate for the Young's modulus of both the smooth and nubbed shell with a linear elastic material. The range of validity will be highly dependent on the diameter, shell thickness and imperfections of the sphere. This relation was not studied in great detail and should only be used as an indication that this approach might be applicable for HILE spheres.

5.3.2 Simplified Nubbed Shell

The simplified nubbed shells were very useful in the sensitivity study of the HILE material. They significantly reduced run time and enabled fast iterations across parameters. Their applicability with the Yeoh material is questionable as the calibration between the nubbed and simple sections will become very complex. Their usefulness will therefor be limited.

5.3.3 Nubbed Shell

Ideally the NPs and surfactant shell would have been modeled with unique material parameters. Assigning the NPs a unique material was not trivial to automate and the homogeneous model was therefore adopted. The rapid increase in thickness at the edge of the NPs mean that most of the deformation occurs in the thinner shell between the NPs. The geometric effect of the NPs plate contact is maintained due to the limited deformation and flattening of the solid NPs. Inter NP deformations are assumed to be a greater issue in the Yeoh model due to the low initial stiffness. This again reinforces the notion that they should have been modeled with different properties.

The NP packing density chosen was based on visual inspection of the SEM images in Section 2.1.3. There appears to be some separation between the smaller NPs. It was attempted to count the number of fluorescent particles seen in Figure 2.4 and guessing the diameter being the MB size average, $3\mu m$. A $D_{MB} = 3.0\mu m$ model with a $Q = 60$ packing density has about the same number of particles in it's symmetry plane as the fluorescent MB. Also considering the small repulsive force caused by the negative ζ potential the NPs were placed some distance apart. In hindsight this was a premature decision due to the uncertainty of the reference diameter and a larger variety of packing densities should have been tried. The SEM images can also have been wrongly interpreted and the perceived separation might also be a product the protein surfactant filling the voids between the NPs in a non-uniform way.

A simulation problem that will arise with the denser NP packing is the equidistant distribution. The Fibonacci lattice sees a slightly denser packing in one particular direction. If the homogeneous material model is employed as packing density increases, the touching NPs will form continuous spirals extending from the lattice poles. This spiral will be thicker than the shell itself, inducing a stiffer behaviour. The Fibonacci method also does not pack the NPs as efficiently as possible. It is believed that a unstructured distribution could yield a denser lower packing limit. This could potentially be done by solving the Thompson model presented in Section 3.5.1. This could prove to be computationally expensive and other more efficient methods might be available.

As mentioned previously, thinner shells should also have been further investigated. The lower estimate for a pure HSA bubble ($15nm$) should also have been included. This was not accomplished due to the modeling method and the large number of elements required to run the model.

The contact between the compressing plate and the NP-MP was modeled frictionless. As mentioned in Section 4.4 some MBs exhibit a binding effect, which is the MB sticking to the AFM tip. This indicates that the contact maybe should not be modeled frictionless.

5.3.4 Alternative Modeling Method

An alternative modeling method was hypothesized late in the project. This was not tested but might yield better results. It is based on creating a second set of NPs as surface based parts, separate from the the full NP-MB model. By using a Boolean cut between a concentric NP surface and an embedded NP, a separate part will be created where the solid NP is now

a unique segment contained in the full model. Using this method on all the NPs we can assign a unique material parameter to each. This would allow us to increase the mesh size in the solid NP segments, reducing run time. Appropriate material properties can now also be assigned the NPs, eliminating any unrealistic deformation happening within the NP. This could potentially be combined with discrete rigid surfaces, further reducing computational cost.

5.4 Estimating Viscosity of NP-MB Shell

Estimating the viscosity of the NP-MB shell based on the $F-\Delta$ hysteresis resulted in a significantly higher shear viscosity than previously estimated by Finnøy. The validity of this thesis' assumptions must be further investigated. An explanation could also be caused by equipment specific properties like a hysteresis in the z-measurement of the AFM base location. Finnøys measurements were run with a closed Z loop which compensates for any hysteresis in the piezo element controlling the z axis motion. It is not known if Moe employed the same method but $F-\Delta$ hysteresis is seen in both Finnøy's and Moe's experiments. The shell viscosity estimation used by Finnøy and Moe has used by several other [62, 63, 64, 65]. It is based on a indirect measurement. This is something that will induce further uncertainty as the indirect measurements adds another layer of potential errors. The attenuation is measured when a MB solution is exposed to a varying ultrasound field. The results are then compared to analytically developed attenuation curves from which a shell viscosity can be inferred. The frequency the MBs are exposed to in the attenuation estimates are also much larger than the AFM compression. The viscosity could potentially be rate dependent.

5.5 Implications and Further Work

We have shown that the Yeoh material model better predicts the $F-\Delta$ response of a NP-MB. Based on the data available it was not possible to definitely conclude that this is the primary cause of non-linearity. The Yeoh models applicability should be confirmed by using it on a sample size with a larger deformation regime.

Attenuation

If the Yeoh material model is applicable we can investigate the effect this has on the analytical estimates of the attenuation as an MB is exposed to a acoustic pressure. The dynamic equations used to simulate a theoretical attenuation elastic shell bubbles, Church [66] and the thin shell version presented by Hoff et al. [67], incorporate a linear elastic material for non-linear oscillations. We suggest expanding the equations to consider the non-linear stress strain relation of the Yeoh model. The established analytical solution to the non-linear problem is then voided but the response for a given system can still be numerically integrated. This can then be compared to the linear material models and the measured attenuation.

Shell Thickness

Regardless of the material model used in either quasi-static or dynamic considerations of MB properties, the challenge of determining the shell thickness remains. The method of estimating the shell thickness as a function of the buckling point is promising. In order for this to be useful it should be expanded with the Yeoh material model and run for a larger variety of parameter. First and foremost thinner shells should be simulated as this seems to be a very relevant factor. Presently only the MB diameter and shell thickness are included, but this should be expanded to include all relevant parameters. Finding the appropriate parameters values when the parameter functions are seemingly discontinuous will be a challenge. The assumption that a single parameters response is independent of the other parameters will also have to be investigated.

Reissner Theory

The linearity of the large deformation plate loading of both the smooth and irregular surface shell was somewhat surprising. This is an extension of the finite element analysis Elsner et al.[21] conducted on the Reissner Theory's validity for a rigid sphere compression of a spherical shell. The rigid sphere had a radius four times larger than the shell being compressed. Our simulations are conceptually similar but with an infinite radius on the compressing sphere. This has not the primary focus of the thesis and should thus be further investigated for validity.

5.5.1 Alternative Method for Determinig NP-MB Tensile Modulus

Investigating the basis for the deJong theory presented in 1.5.1 and its incompatibility with the AFM experiment spurred the idea of utilizing this theory on a applicable experiment. An alternative method for determining the shell parameters is suggested. This method, hereby referred to as Morton's method, is motivated by the deJong theory where the bubble radius is a function a induced hydrostatic pressure. The hypothesis is that large quantities of relatively accurate of data can be obtained with little equipment other than an accurate microscope with imaging capabilities. By subjecting a MB solution to a hydrostatic pressure we can relate the change of radius to the imposed pressure and hence gain insight of the shells properties.

Previously the deJong theory has only been used to estimate the response and attenuation of MBs exposed to an acoustic pressure. The acoustic pressure is often in the MHz range meaning the response needs to be considered dynamic. The concept of tracking MB diameter with the purpose of determining shell parameters has previously only been done by high speed imaging of the response to an acoustic pressure [68, 69]. By not using the acoustic pressure as the exiting force we reduce potential errors associated with the dynamic response of the bubble.

Having the ability to accurately image MBs in a solution allows us to determine the radius of the MBs in the field of view. By imaging the MBs before and after a hydrostatic pressure has been applied we can determine shell properties like the thickness and stiffness. The number of data points gathered from each experiment will be a function of the numbers of NPs in the field of view. Initial analysis of the response can be determined manually as a proof of concept. By employing an image analyzing algorithm this experimental method can be automated and scaled. This will enable statistical analysis of the data, which will be useful in characterizing general MB properties and predicting typical behaviour. There has not been found any previous literature on utilizing a hydrostatic pressure and the radial response of an MB to establish shell properties. deJong et al. (2009)[68] used a high speed camera to image the bubble response as a function of an acoustic pulse. Marmottant et al. [70] investigated the critical buckling pressure of a coated MB. This will be relevant when MBs are exposed to an overpressure.

Practical Considerations

In order to get a quasi-static radial response the MBs must be exposed to a hydrostatic pressure. This means that the MBs must be contained in a pressure vessel. As far as initial research can tell there is no available system which can impose a hydrostatic pressure on a sample while maintaining the ability to image the sample. This will be an engineering challenge as the quality of the microscope image is dependent on the glass thickness of the sample container.

The thin glass surface poses a limitation as maximum operating pressure will be a function of the thickness and surface are of the glass. An initial analytical consideration indicates that a 1mm thick glass plate covering a 30mm diameter hole will be able to withstand about 200kPa before breaking. This means that the unsupported glass surface should be as small as possible while still allowing the microscope aperture to contact the glass of the sample container. The aperture requires direct contact with the sample container and a small drop of oil is used to ensure the desired optical qualities of the interface. The MBs will also have to be immobilised on the glass surface as a larger than necessary focal distance will impact the accuracy. Immobilization is described in Finnøy's thesis [41].

The imaging equipment available at the Department of Physics has a resolution of 150nm. Initial consideration of a NP-MB similar to the GB bubbles $D_{MB} = 3.0\mu m,\ t = 0.05\mu m$ give an idea about the expected response. The low initial stiffness of the bubble deformations is translated into an visually estimated initial tensile stiffness $E = 5MPa$. This gives an expected change in diameter of $4.5nm/kPa$. If the Yeoh material model better represent the actual behavior then this ratio will increase due to a lower initial stiffness.

In addition to an imaging system a pressure vessel and a pump is required. The pump should be able to create both under- and overpressure and does not need to be sophisticated beyond keeping a constant pressure. An accurate pressure gauge is also required. If we want to follow the slow dynamic response of the bubble a data logging tool would be needed for the pressure gauge.

Morton's method remains to be tested but hopefully this will be an efficient and accurate way of estimating shell properties for quasi-static loading. The only larger, more expensive, equipment required is the microscope making it easy to use as no high speed camera is required. Capturing many data samples in each experiment will enable the use of statistical tool which enables better and more general characterization.

Chapter 6

Conclusion

This thesis has shown that finite element simulation can be used to estimate shell properties of a nanoparticle-stabilized microbubble. The Yeoh parameter is a better fit to the experimental data than the linear elastic material. The piecewise linear regions present in many of the NP-MB $F-\Delta$ curves are unfortunately not represented by the Yeoh model's simulated response. Based on this we can conclude that a non-linear behavior of the material is a likely but not necessarily exclusive factor of the non-linear response seen in the experimental data. The HILE material simulations showed no sign of stiffening. This presumably leaves any undetermined boundary conditions as the sole cause of the non-linear response. Based on the large deformations of the bubbles it is not likely that the unknown boundary conditions are the sole perpetrator either. We therefore conclude that it is unlikely that the material properties behave linearly. The introduction of the non-linear tensile modulus might impact the results of current analytical estimates pertaining to a protein MB shell exposed to an acoustic pressure.

The FE models also allows us to extract information based the buckling point of the MBs. Until a better approach for estimating an NP-MBs shell thickness is devised, our suggested method will hopefully be a valuable improvement over the previously utilized educated guess.

The proposed method of estimating the shell viscosity based on the loading curve hysteresis is not deemed suitable. This is due to the large discrepancy between the estimated viscosities and previously reported viscosities.

Bibliography

[1] Gard Fostad Moe. *Mechanical and Acoustic Characterization of Perfluorocarbon Microbubbles Containing Nanoparticles*. PhD thesis, NTNU, 2015.

[2] Remon Bazak, Mohamad Houri, Samar El Achy, Wael Hussein, and Tamer Refaat. Passive targeting of nanoparticles to cancer: A comprehensive review of the literature. *Molecular and clinical oncology*, 2(6):904–908, nov 2014.

[3] Jörg Kreuter. Nanoparticles–a historical perspective. *International journal of pharmaceutics*, 331(1):1–10, feb 2007.

[4] Khaled Greish. Enhanced permeability and retention (EPR) effect for anticancer nanomedicine drug targeting. *Methods in molecular biology (Clifton, N.J.)*, 624:25–37, jan 2010.

[5] Yinan Zhong, Fenghua Meng, Chao Deng, and Zhiyuan Zhong. Ligand-directed active tumor-targeting polymeric nanoparticles for cancer chemotherapy. *Biomacromolecules*, 15(6):1955–69, jun 2014.

[6] Theresa M Allen. Ligand-targeted therapeutics in anticancer therapy. *Nature reviews. Cancer*, 2(10):750–63, oct 2002.

[7] David Lembo and Roberta Cavalli. Nanoparticulate delivery systems for antiviral drugs. *Antiviral chemistry & chemotherapy*, 21(2):53–70, jan 2010.

[8] David Cosgrove. Ultrasound contrast agents: an overview. *European journal of radiology*, 60(3):324–30, dec 2006.

[9] Fikri M Abu-Zidan, Ashraf F Hefny, and Peter Corr. Clinical ultrasound physics. *Journal of emergencies, trauma, and shock*, 4(4):501–3, oct 2011.

[10] S. R. Sirsi and M. A. Borden. Microbubble compositions, properties and biomedical applications. *Bubble Science, Engineering & Technology*, 1(1-2):3–17, nov 2009.

[11] Jonathan R Lindner, Ji Song, Ananda R Jayaweera, Jiri Sklenar, and Sanjiv Kaul. Microvascular rheology of Definity microbubbles after intra-arterial and intravenous administration. *Journal of the American Society of Echocardiography : official publication of the American Society of Echocardiography*, 15(5):396–403, may 2002.

[12] Andreas K O Åslund, Sigrid Berg, Sjoerd Hak, Ýrr Mørch, Sverre H Torp, Axel Sandvig, Marius Widerøe, Rune Hansen, and Catharina de Lange Davies. Nanoparticle delivery to the brain - By focused ultrasound and self-assembled nanoparticle-stabilized microbubbles. *Journal of controlled release : official journal of the Controlled Release Society*, 220(Pt A):287–294, oct 2015.

[13] Siv Eggen, Stein-Martin Fagerland, Ýrr Mørch, Rune Hansen, Kishia Søvik, Sigrid Berg, Håkon Furu, Audun Dybvik Bøhn, Magnus B Lilledahl, Anders Angelsen, Bjørn Angelsen, and Catharina de Lange Davies. Ultrasound-enhanced drug delivery in prostate cancer xenografts by nanoparticles stabilizing microbubbles. *Journal of controlled release : official journal of the Controlled Release Society*, 187:39–49, aug 2014.

[14] N. de Jong, L. Hoff, T. Skotland, and N. Bom. Absorption and scatter of encapsulated gas filled microspheres: Theoretical considerations and some measurements. *Ultrasonics*, 30(2):95–103, mar 1992.

[15] H Reismann and PS Pawlik. *Elasticity: Theory and application*. Wiley, 1980.

[16] Cherry C Chen, Shih-Ying Wu, John D Finan, Barclay Morrison, and Elisa E Konofagou. An experimental study on the stiffness of size-isolated microbubbles using atomic force microscopy. *IEEE transactions on ultrasonics, ferroelectrics, and frequency control*, 60(3):524–34, mar 2013.

[17] Julia Kathleen Morris. *Mechanical properties of phospholipid coated microbubbles*. PhD thesis, nov 2014.

[18] Eric Reissner. Stresses and Small Displacements of Shallow Spherical Shells. I. *Journal of Mathematics and Physics*, 25(1-4):80–85, apr 1946.

[19] Eric Reissner. Stresses and Small Displacements of Shallow Spherical Shells. II. *Journal of Mathematics and Physics*, 25(1-4):279–300, apr 1946.

[20] Emmanouil Glynos, Vasileios Koutsos, W Norman McDicken, Carmel M Moran, Stephen D Pye, James A Ross, and Vassilis Sboros. Nanomechanics of biocompatible hollow thin-shell polymer microspheres. *Langmuir : the ACS journal of surfaces and colloids*, 25(13):7514–22, jul 2009.

[21] N Elsner, F Dubreuil, and R Weinkamer. Mechanical properties of freestanding polyelectrolyte capsules: a quantitative approach based on shell theory. *... of Polymer Surfaces ...*, 2006.

[22] Evelyn Buchner Santos, Julia K Morris, Emmanouil Glynos, Vassilis Sboros, and Vasileios Koutsos. Nanomechanical properties of phospholipid microbubbles. *Langmuir : the ACS journal of surfaces and colloids*, 28(13):5753–60, apr 2012.

[23] Alkmini Lytra, Nikos Pelekasis, Vassilis Sboros, Emmanouil Glynos, and Vasileios Koutsos. Static Response of Coated Microbubbles: Modeling Simulations and Parameter Estimation. *Procedia IUTAM*, 16:123–133, 2015.

[24] WC Young and RG Budynas. *Roark's formulas for stress and strain*. McGraw-Hill, 2002.

[25] Valentin Lulevich, Tiffany Zink, Huan-Yuan Chen, Fu-Tong Liu, and Gang-Yu Liu. Cell mechanics using atomic force microscopy-based single-cell compression. *Langmuir : the ACS journal of surfaces and colloids*, 22(19):8151–5, sep 2006.

[26] Valentin V Lulevich, Denis Andrienko, and Olga I Vinogradova. Elasticity of polyelectrolyte multilayer microcapsules. *The Journal of chemical physics*, 120(8):3822–6, feb 2004.

[27] Ýrr Mørch, Rune Hansen, Sigrid Berg, Andreas K O Åslund, Wilhelm R Glomm, Siv Eggen, Ruth Schmid, Heidi Johnsen, Stephan Kubowicz, Sofie Snipstad, Einar Sulheim, Sjoerd Hak, Gurvinder Singh, Birgitte H McDonagh, Hans Blom, Catharina de Lange Davies, and Per M Stenstad. Nanoparticle-stabilized microbubbles for multimodal imaging and drug delivery. *Contrast media & molecular imaging*, 10(5):356–66, jan 2015.

[28] Mark A. Borden and Marjorie L. Longo. Dissolution Behavior of Lipid Monolayer-Coated, Air-Filled Microbubbles: Effect of Lipid Hydrophobic Chain Length. *Langmuir*, 18(24):9225–9233, nov 2002.

[29] P. S. Epstein and M. S. Plesset. On the Stability of Gas Bubbles in Liquid-Gas Solutions, nov 1950.

[30] M. Azmin, G. Mohamedi, M. Edirisinghe, and E.P. Stride. Dissolution of coated microbubbles: The effect of nanoparticles and surfactant concentration. *Materials Science and Engineering: C*, 32(8):2654–2658, dec 2012.

[31] Stéphanie Pasche, Marcus Textor, Laurence Meagher, Nicholas D. Spencer, and Hans J. Griesser. Relationship between Interfacial Forces Measured by Colloid-Probe Atomic Force Microscopy and Protein Resistance of Poly(ethylene glycol)-Grafted Poly(l -lysine) Adlayers on Niobia Surfaces. *Langmuir*, 21(14):6508–6520, jul 2005.

[32] D. Kowalczyk, J. P. Marsault, and S. Slomkowski. Atomic force microscopy of human serum albumin (HSA) on poly(styrene/acrolein) microspheres. *Colloid & Polymer Science*, 274(6):513–519, jun 1996.

[33] N. Sponheim, L. Hoff, A. Waaler, B. Muan, H. Morris, S. Holm, M. Myrum, N. de Jong, and T. Skotland. Acoustic Sensing and Imaging, 1993., International Conference on, 1993.

[34] J Barnhart, H Levene, E Villapando, J Maniquis, J Fernandez, S Rice, E Jablonski, T Gjøen, and H Tolleshaug. Characteristics of Albunex: air-filled albumin microspheres for echocardiography contrast enhancement. *Investigative radiology*, 25 Suppl 1:S162–4, sep 1990.

[35] Hans-Jürgen Butt, Brunero Cappella, and Michael Kappl. Force measurements with the atomic force microscope: Technique, interpretation and applications. *Surface Science Reports*, 59(1-6):1–152, oct 2005.

[36] J. E. McKendry, C. A. Grant, B. R. G. Johnson, P. L. Coletta, J. A. Evans, and S. D. Evans. Force spectroscopy of streptavidin conjugated lipid coated microbubbles. *Bubble Science, Engineering & Technology*, 2(2):48–54, may 2010.

[37] Jan Domke and Manfred Radmacher. Measuring the Elastic Properties of Thin Polymer Films with the Atomic Force Microscope. *Langmuir*, 14(12):3320–3325, jun 1998.

[38] R E Mahaffy, S Park, E Gerde, J Käs, and C K Shih. Quantitative analysis of the viscoelastic properties of thin regions of fibroblasts using atomic force microscopy. *Biophysical journal*, 86(3):1777–93, mar 2004.

[39] Michael J Jaasma, Wesley M Jackson, and Tony M Keaveny. Measurement and characterization of whole-cell mechanical behavior. *Annals of biomedical engineering*, 34(5):748–58, may 2006.

[40] Abraham. Savitzky and M. J. E. Golay. Smoothing and Differentiation of Data by Simplified Least Squares Procedures. *Analytical Chemistry*, 36(8):1627–1639, jul 1964.

[41] Andreas Finnøy. Acoustic and Mechanical Properties of Microbubbles Stabilized by Polymeric Nanoparticles, 2013.

[42] Jonathan Ophir, S. Kaisar Alam, Brian S. Garra, Faouzi Kallel, Elisa E. Konofagou, Thomas Krouskop, Christopher R. B. Merritt, Raffaella Righetti, Remi Souchon, Seshadri Srinivasan, and Tomy Varghese. Elastography: Imaging the elastic properties of soft tissues with ultrasound. *Journal of Medical Ultrasonics*, 29(4):155–171, dec 2002.

[43] EJ Chen and J Novakofski. Young's modulus measurements of soft tissues with application to elasticity imaging. ... *and Frequency Control* ..., 1996.

[44] Wolfgang Schmidt and Georg Roessling. Novel manufacturing process of hollow polymer microspheres. *Chemical Engineering Science*, 61(15):4973–4981, aug 2006.

[45] Felix Rico, Annafrancesca Rigato, Laura Picas, and Simon Scheuring. Mechanics of proteins with a focus on atomic force microscopy. *Journal of nanobiotechnology*, 11 Suppl 1(1):S3, jan 2013.

[46] Hiroshi Sekiguchi, Hideo Arakawa, Hideki Taguchi, Takeshi Ito, Ryohei Kokawa, and Atsushi Ikai. Specific interaction between GroEL and denatured protein measured by compression-free force spectroscopy. *Biophysical journal*, 85(1):484–90, jul 2003.

[47] Chih-Kung Lee, Yu-Ming Wang, Long-Sun Huang, and Shiming Lin. Atomic force microscopy: determination of unbinding force, off rate and energy barrier for protein-ligand interaction. *Micron (Oxford, England : 1993)*, 38(5):446–61, jan 2007.

[48] P Hinterdorfer, W Baumgartner, H J Gruber, K Schilcher, and H Schindler. Detection and localization of individual antibody-antigen recognition events by atomic force microscopy. *Proceedings of the National Academy of Sciences of the United States of America*, 93(8):3477–81, apr 1996.

[49] Masaru Kawakami, Katherine Byrne, David J Brockwell, Sheena E Radford, and D Alastair Smith. Viscoelastic study of the mechanical unfolding of a protein by AFM. *Biophysical journal*, 91(2):L16–8, jul 2006.

[50] J.J. Thomson. XXIV. On the structure of the atom: an investigation of the stability and periods of oscillation of a number of corpuscles arranged at equal intervals around the circumference of a circle; with application of the results to the theory of atomic structure. *Philosophical Magazine Series 6*, 7(39):237–265, mar 1904.

[51] EA Rakhmanov, EB Saff, and YM Zhou. Minimal discrete energy on the sphere. *Math. Res. Lett*, 1994.

[52] Álvaro González. Measurement of Areas on a Sphere Using Fibonacci and Latitude–Longitude Lattices. *Mathematical Geosciences*, 42(1):49–64, nov 2010.

[53] Helmut Vogel. A better way to construct the sunflower head. *Mathematical Biosciences*, 44(3-4):179–189, jun 1979.

[54] B Keinert and M Innmann. Spherical fibonacci mapping. *ACM Transactions on ...*, 34(6):193:1–193:7, 2015.

[55] Srinivas C Tadepalli, Ahmet Erdemir, and Peter R Cavanagh. Comparison of hexahedral and tetrahedral elements in finite element analysis of the foot and footwear. *Journal of biomechanics*, 44(12):2337–43, aug 2011.

[56] Dassault Systèmes. Abaqus Analysis User's Guide, 2013.

[57] AV Pogorelov. *Bendings of surfaces and stability of shells*. American Mathematical Soc., 1988.

[58] Phadungath Chanokphat. Casein micelle structure: A concise review. *Songklanakarin Journal of Science and Technology*, 27(1), jan 2005.

[59] N. Somanathan, V. Arumugam, and R. Sanjeevi. Mechanical properties and temperature dependence of grafted casein films. *European Polymer Journal*, 23(10):803–807, jan 1987.

[60] U Kragh-Hansen. Structure and ligand binding properties of human serum albumin. *Danish medical bulletin*, 37(1):57–84, feb 1990.

[61] Alimjan Idiris, Satoru Kidoaki, Kengo Usui, Tei Maki, Harukazu Suzuki, Masayoshi Ito, Makoto Aoki, Yoshihide Hayashizaki, and Takehisa Matsuda. Force Measurement for AntigenAntibody Interaction by Atomic Force Microscopy Using a Photograft-Polymer Spacer. *Biomacromolecules*, 6(5):2776–2784, sep 2005.

[62] Alexander A Doinikov, Jillian F Haac, and Paul A Dayton. Modeling of nonlinear viscous stress in encapsulating shells of lipid-coated contrast agent microbubbles. *Ultrasonics*, 49(2):269–75, feb 2009.

[63] L. Hoff. *Acoustic Characterization of Contrast Agents for Medical Ultrasound Imaging*. Springer Science & Business Media, 2001.

[64] Miguel A Parrales, Juan M Fernandez, Miguel Perez-Saborid, Jonathan A Kopechek, and Tyrone M Porter. Acoustic characterization of monodisperse lipid-coated microbubbles: relationship between size and shell viscoelastic properties. *The Journal of the Acoustical Society of America*, 136(3):1077, sep 2014.

[65] E Stride, K Pancholi, M J Edirisinghe, and S Samarasinghe. Increasing the nonlinear character of microbubble oscillations at low acoustic pressures. *Journal of the Royal Society, Interface / the Royal Society*, 5(24):807–11, jul 2008.

[66] Charles C. Church. The effects of an elastic solid surface layer on the radial pulsations of gas bubbles. *The Journal of the Acoustical Society of America*, 97(3):1510, 1995.

[67] Lars Hoff, Per C. Sontum, and Jens M. Hovem. Oscillations of polymeric microbubbles: Effect of the encapsulating shell. *The Journal of the Acoustical Society of America*, 107(4):2272, 2000.

[68] Nico de Jong, Marcia Emmer, Annemieke van Wamel, and Michel Versluis. Ultrasonic characterization of ultrasound contrast agents. *Medical & biological engineering & computing*, 47(8):861–73, aug 2009.

[69] Juan Tu, Jingfeng Guan, Yuanyuan Qiu, and Thomas J Matula. Estimating the shell parameters of SonoVue microbubbles using light scattering. *The Journal of the Acoustical Society of America*, 126(6):2954–62, dec 2009.

[70] Philippe Marmottant, Ayache Bouakaz, Nico de Jong, and Catherine Quilliet. Buckling resistance of solid shell bubbles under ultrasound. *The Journal of the Acoustical Society of America*, 129(3):1231–9, mar 2011.

Appendix A

AFM Data from Finnøy

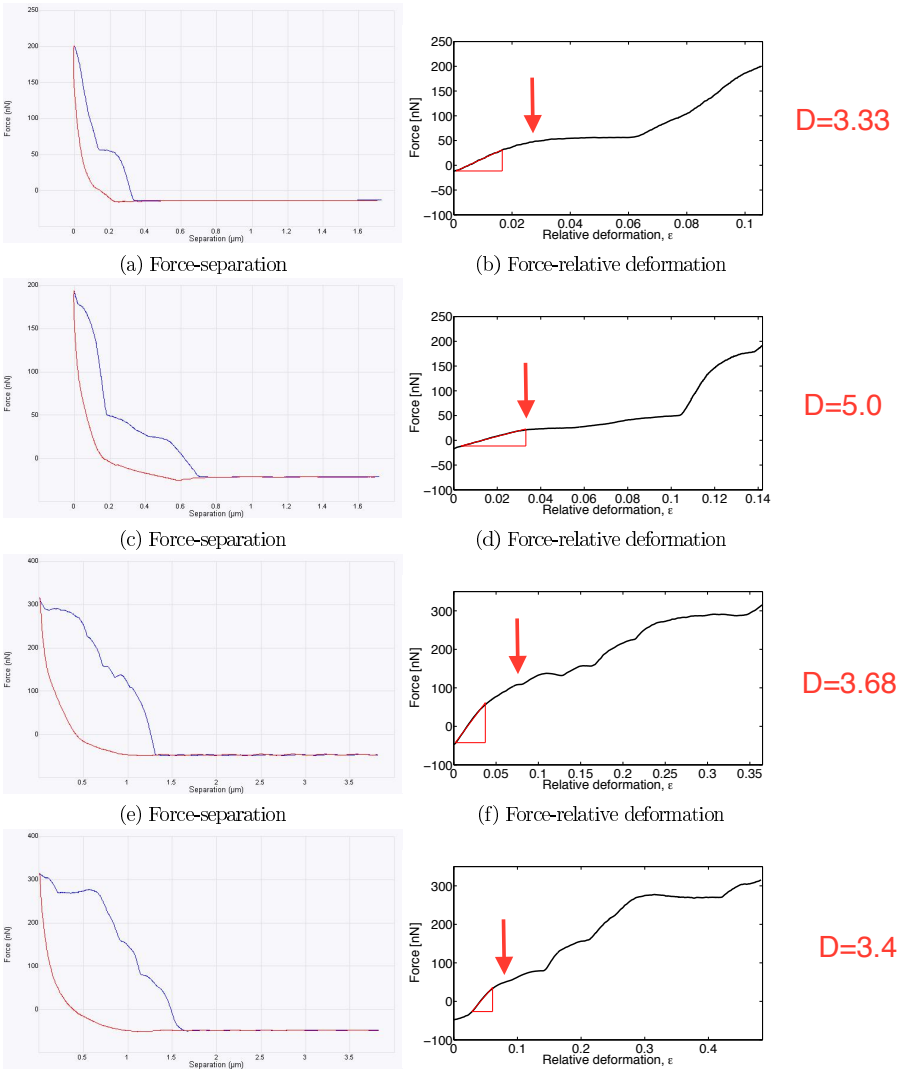

(a) Force-separation (b) Force-relative deformation

(c) Force-separation (d) Force-relative deformation

(e) Force-separation (f) Force-relative deformation

(g) Force-separation (h) Force-relative deformation

Figure 4.19: Force-separation curves and force-relative deformation curves obtained from a selection of compressed microbubbles stabilized by YM-44 and BSA

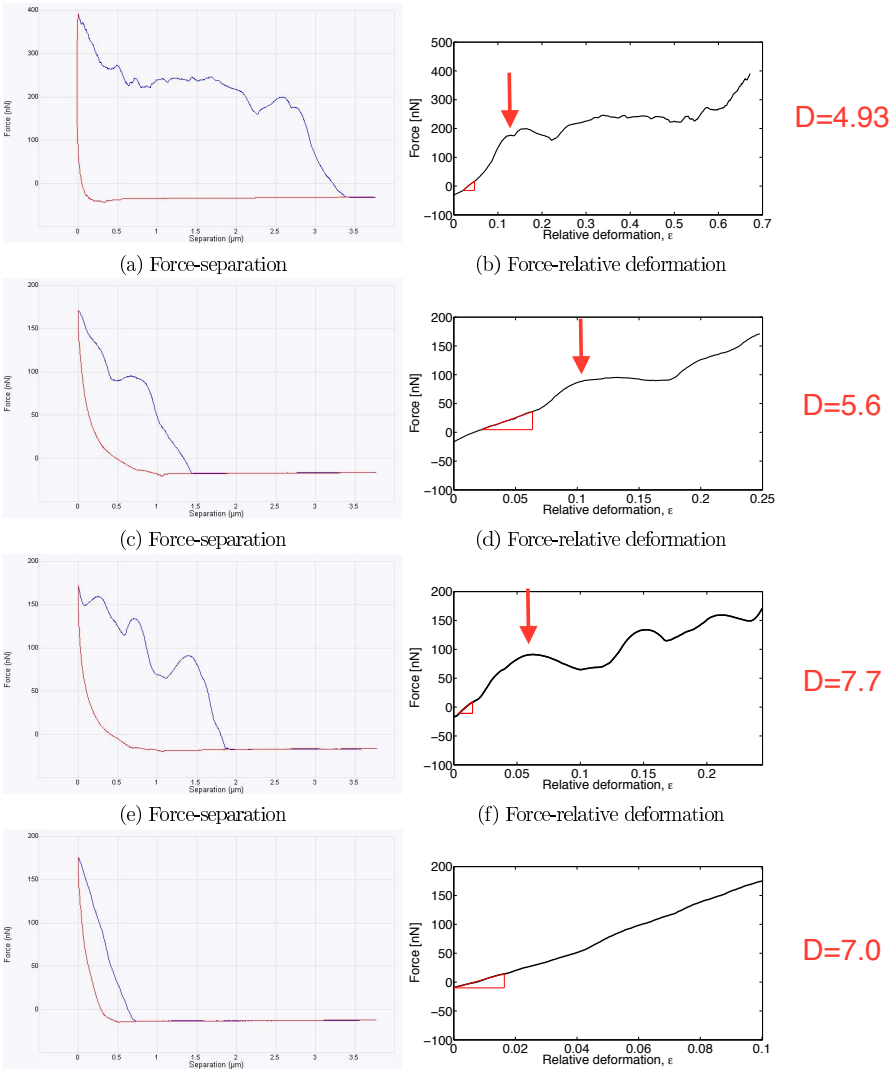

(a) Force-separation (b) Force-relative deformation

(c) Force-separation (d) Force-relative deformation

(e) Force-separation (f) Force-relative deformation

(g) Force-separation (h) Force-relative deformation

Figure 4.20: Force-separation curves and force-relative deformation curves obtained from a selection of compressed microbubbles stabilized by YM-73 and BSA

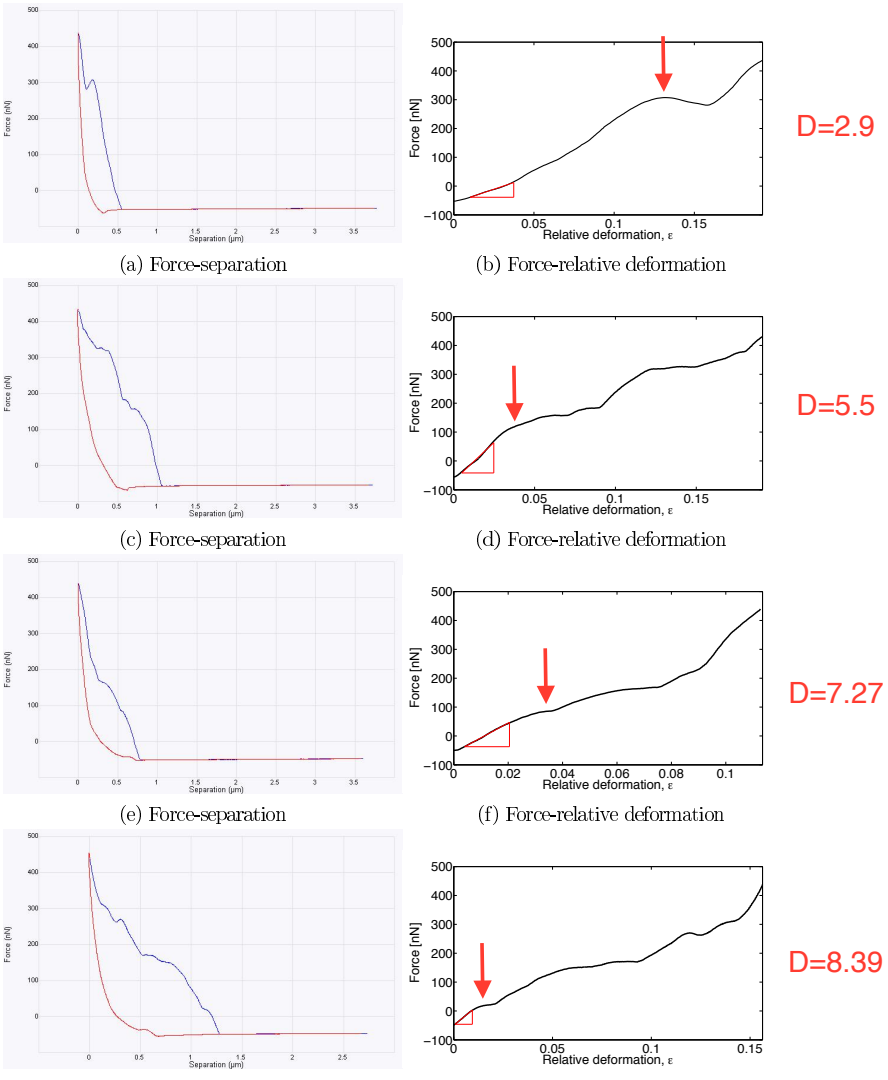

(a) Force-separation (b) Force-relative deformation

(c) Force-separation (d) Force-relative deformation

(e) Force-separation (f) Force-relative deformation

(g) Force-separation (h) Force-relative deformation

Figure 4.21: Force-separation curves and force-relative deformation curves obtained from a selection of compressed microbubbles stabilized by YM-73 and casein.